SHELL-CORRECTION METHODS FOR CLUSTERS:
Theory and applications

C. YANNOULEAS AND UZI LANDMAN
School of Physics, Georgia Institute of Technology
Atlanta, Georgia 30332-0430, USA

1 Introduction

One of the principle themes in research on finite systems (e.g., nuclei, atomic and molecular clusters, and nano-structured materials) is the search for size-evolutionary patterns (SEPs) of properties of such systems and elucidation of the physical principles underlying such patterns [1].

Various physical and chemical properties of finite systems exhibit SEPs, including:

1. Structural characteristics pertaining to atomic arrangements and particle morphologies and shapes;
2. Excitation spectra involving bound-bound transitions, ionization potentials (IPs), and electron affinities (EAs);
3. Collective excitations (electronic and vibrational);
4. Magnetic properties;
5. Abundance spectra and stability patterns, and their relation to binding and cohesion energetics, and to the pathways and rates of dissociation, fragmentation, and fission of charged clusters;
6. Thermodynamic stability and phase changes;
7. Chemical reactivity.

The variations with size of certain properties of materials aggregates are commonly found to scale with the surface to volume ratio of the cluster, i.e., $S/\Omega \sim R^{-1} \sim N^{1/3}$, where S, Ω, R, and N are the surface area, volume, average radius, and number of particles, respectively (even when applicable, the physical origins of such scaling may vary for different properties). However, characterization of SEPs in finite systems in terms of such

T. P. Martin (ed.), Large Clusters of Atoms and Molecules, 131–200.

scaling is non-universal, in the sense of properties whose SEPs are of different physical origins; e.g., magic-number patterns and odd-even oscillations characteristic to metal clusters (portrayed in non-monotonic abundance distributions and ionization potential spectra, and in energetics and barrier profiles and heights for fission of charged metal clusters) whose origins are related to electronic shell structure rather than to surface-to-volume considerations.

Nevertheless, in many occasions, even for the aforementioned ones, it is convenient to analyze the energetics of finite systems in terms of two contributions, namely, (i) a term which describes the energetics as a function of the system size in an average sense (not including shell-closure effects), referrred to usually as describing the "smooth" part of the size dependence, and (ii) an electronic shell-correction term. The first term is the one which is expected to vary smoothly and be expressible as an expansion in S/Ω, while the second one contains the characteristic oscillatory patterns as the size of the finite system is varied. Such a strategy has been introduced [2] and often used in studies of nuclei [3], and has been adopted recently for investigations of metal clusters ([4]-[13]) and fullerenes [14]. As a motivating example we show in Fig. 1 the SEP of the IPs of Na_N clusters, which illustrates odd-even oscillations in the observed spectrum, a smooth description of the pattern [Fig. 1(a)], and two levels of shell-corrected descriptions — one assuming spherical symmetry [Fig. 1(b)], and the other allowing for triaxial shape deformations [Fig. 1(c)]. The progressive improvement of the level of agreement between the experimental and theoretical patterns is evident.

In these lectures, we review the development of shell-correction methods (SCM), and illustrate their applications to atomic and molecular cluster-systems. The text is organized as folllows. In section 2, the methodology of shell-correction methods is described, and a microscopic local-density-functional-approximation SCM (LDA-SCM) is derived and applied to investigations of the stability and decay channels of multiply charged metal clusters and fullerenes. In section 3, semi-empirical SCM (SE-SCM) methods are described and anisotropic oscillator models are developed and used in investigations of SEPs of the properties of neutral and charged metal clusters (such as IPs, EAs, fission energetics, and monomer and dimer separation energies) including analysis of triaxial shape deformations which are found to underlie the appearance of odd-even alternations of certain properties as a function of cluster size. Additionally, the influence of electronic shell effects on barriers and channels of cluster fission are discussed using a shell correction method in conjunction with an asymmetric two-

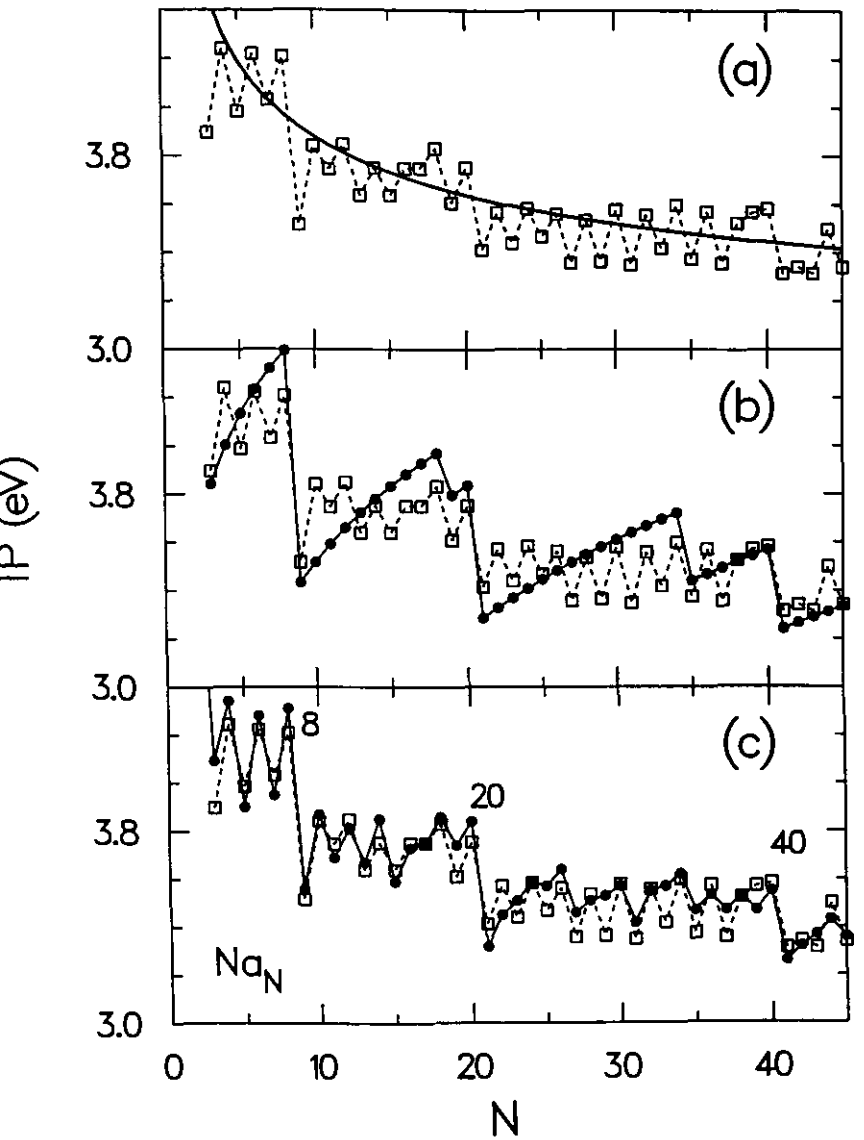

Fig. 1. IPs of Na_N clusters. Open squares: Experimental measurements of Ref. [106]. The solid line at the top panel (a) represents the smooth contribution to the theoretical total IPs. The solid circles in the middle (b) and bottom (c) panels are the total SCM IPs. The shapes of sodium clusters have been assumed spherical in the middle panel, while triaxial deformations have been considered at the bottom one.

center-oscillator potential model.

2 Shell-correction methodology and microscopic LDA-SCM

2.1 Methodology and derivation of LDA-SCM

2.1.1 Historical review of SCM

It has long been recognized in nuclear physics that the dependence of ground-state properties of nuclei on the number of particles can be viewed as the sum of two contributions: the first contribution varies smoothly with the particle number (number of protons N_p and neutrons N_n) and is referred to as the *smooth* part; the second contribution gives a superimposed structure on the smooth curve and exhibits an oscillatory behavior, with extrema at the nuclear magic numbers [15, 3].

Nuclear masses have provided a prototype for this behavior [15]. Indeed, the main contributions to the experimental nuclear binding energies are smooth functions of the number of protons and neutrons, and are described by the semi-empirical mass formula [16, 17]. The presence of these smooth terms led to the introduction of the liquid-drop model (LDM), according to which the nucleus is viewed as a drop of a nonviscous fluid whose total energy is specified by volume, surface, and curvature contributions [15, 3, 18].

The deviations of the binding energies from the smooth variation implied by the LDM have been shown [18, 2] to arise from the shell structure associated with the bunching of the discrete single-particle spectra of the nucleons, and are commonly referred to as the shell correction. Substantial progress in our understanding of the stability of strongly deformed open-shell nuclei and of the dynamics of nuclear fission was achieved when Strutinsky proposed [2] a physically motivated efficient way of calculating the shell corrections. The method consists of averaging (see below) the single-particle spectra of phenomenological deformed potentials and of subtracting the ensuing average from the total sum of single-particle energies.

While certain analogies, portrayed in experimental data, between properties of nuclei and elemental clusters have been recognized, the nuclear-physics approach of separating the various quantities as a function of size into a smooth part and a shell correction part has only partially been explored in the case of metal clusters. In particular, several investigations ([19]-[22]) had used the ETF method in conjunction with the jellium ap-

proximation to determine the average (smooth, in the sense defined above) behavior of metal clusters, but had not pursued a method for calculating the shell corrections.

In the absence of a method for appropriately calculating shell-corrections for metal clusters in the context of the semiclassical ETF method, it had been presumed that the ETF method was most useful for larger clusters, since the shell effects diminish with increasing size. Indeed, several studies had been carried out with this method addressing the asymptotic behavior of ground-state properties towards the behavior of a jellium sphere of infinite size [23, 24].

It has been observed ([25]-[28]), however, that the single-particle potentials resulting from the semiclassical method are very close, even for small cluster sizes, to those obtained via self-consistent solution of the local density functional approximation (LDA) using the Kohn-Sham (KS) equations [29]. These semiclassical potentials were used extensively to describe the optical (linear) response of spherical metal clusters, for small ([25]-[27]), as well as larger sizes [28] (for an experimental review on optical properties, cf. Refs. [30, 31]). The results of this approach are consistent with time-dependent local density functional approximation (TDLDA) calculations which use the KS solutions [32, 33].

It is natural to explore the use of these semiclassical potentials, in the spirit of Strutinsky's approach, for evaluation of shell corrections in metal clusters of arbitrary size. Below we describe a microscopic derivation of an SCM in conjunction with the local-density functional method ([4]-[6]), and its applications in investigations of the properties of metal clusters and fullerenes. Particularly interesting and promising is the manner by which the shell corrections are introduced by us through the kinetic energy term ([4]-[6]), instead of the traditional Strutinsky averaging procedure of the single-particle spectrum [2]. This is especially desirable, since – unlike the case of atomic nuclei – shell corrections for metal clusters determined by the traditional Strutinsky procedure result in total energies exhibiting substantial systematic deviations from the corresponding KS-LDA energies.

2.1.2 LDA-SCM

Underlying the development of the shell-correction method is the idea of approximating the total energy $E_{total}(N)$ of a finite interacting fermion system as

$$E_{total}(N) = \widetilde{E}(N) + \Delta E_{sh}(N) \,, \qquad (1)$$

where $\widetilde{E}$ is the part that varies smoothly as a function of system size, and ΔE_{sh} is an oscillatory term. Various implementations of such a separation consist of different choices and methods for evaluating the two terms in Eq. (1). Before discussing such methods, we outline a microscopic derivation of Eq. (1).

Motivated by the behavior of the empirical nuclear binding energies, Strutinsky conjectured that the self-consistent Hartree-Fock density ρ_{HF} can be decomposed into a smooth density $\widetilde{\rho}$ and a fluctuating contribution $\delta\rho$, namely $\rho_{HF} = \widetilde{\rho} + \delta\rho$. Then, he proceeded to show that, to second-order in $\delta\rho$, the Hartree-Fock energy is equal to the result that the same Hartree-Fock expression yields when ρ_{HF} is replaced by the smooth density $\widetilde{\rho}$ and the Hartree-Fock single-particle energies ε_i^{HF} are replaced by the single-particle energies corresponding to the smooth potential constructed with the smooth density $\widetilde{\rho}$. Namely, he showed that

$$E_{HF} = E_{Str} + O(\delta\rho^2) \ , \tag{2}$$

where the Hartree-Fock electronic energy is given by the expression

$$E_{HF} = \sum_{i=1}^{occ} \varepsilon_i^{HF} - \frac{1}{2} \int d\mathbf{r} d\mathbf{r}' \mathcal{V}(\mathbf{r} - \mathbf{r}') [\rho_{HF}(\mathbf{r}, \mathbf{r}) \rho_{HF}(\mathbf{r}', \mathbf{r}') - \rho_{HF}(\mathbf{r}, \mathbf{r}')^2] \ , \tag{3}$$

with ε_i^{HF} being the eigenvalues obtained through a self-consistent solution of the HF equation,

$$\left(-\frac{\hbar^2}{2m} \nabla^2 + U_{HF} \right) \phi_i = \varepsilon_i^{HF} \phi_i \ , \tag{4}$$

where

$$U_{HF}(\mathbf{r}) \phi_i(\mathbf{r}) = \int d\mathbf{r}' \mathcal{V}(\mathbf{r} - \mathbf{r}') [\rho_{HF}(\mathbf{r}', \mathbf{r}') \phi_i(\mathbf{r}) - \rho_{HF}(\mathbf{r}', \mathbf{r}) \phi_i(\mathbf{r}')] \ . \tag{5}$$

The Strutinsky approximate energy is written as follows,

$$E_{Str} = \sum_{i=1}^{occ} \widetilde{\varepsilon}_i - \frac{1}{2} \int d\mathbf{r} d\mathbf{r}' \mathcal{V}(\mathbf{r} - \mathbf{r}') [\widetilde{\rho}(\mathbf{r}, \mathbf{r}) \widetilde{\rho}(\mathbf{r}', \mathbf{r}') - \widetilde{\rho}(\mathbf{r}, \mathbf{r}')^2] \ , \tag{6}$$

where the index i in Eqs. (3) and (6) runs only over the occupied states (spin degeneracy is naturally implied). The single-particle energies $\widetilde{\varepsilon}_i$ correspond to a smooth potential $\widetilde{U}$. Namely, they are eigenvalues of a Schrödinger equation,

$$\left(-\frac{\hbar^2}{2m} \nabla^2 + \widetilde{U} \right) \varphi_i = \widetilde{\varepsilon}_i \varphi_i \ , \tag{7}$$

where the smooth potential $\tilde{U}$ depends on the smooth density $\tilde{\rho}$, i.e.,

$$\tilde{U}(\mathbf{r})\varphi_i(\mathbf{r}) = \int d\mathbf{r}' \mathcal{V}(\mathbf{r}-\mathbf{r}')[\tilde{\rho}(\mathbf{r}',\mathbf{r}')\varphi_i(\mathbf{r}) - \tilde{\rho}(\mathbf{r}',\mathbf{r})\varphi_i(\mathbf{r}')] \ , \qquad (8)$$

and $\mathcal{V}$ is the nuclear two-body interaction potential.

It should be noted that while Eqs. (6-8) look formally similar to the Hartree-Fock equations (3-5), their content is different. Specifically, while in the HF equations, the density ρ_{HF} is self-consistent with the wavefunction solutions of Eq. (4), the density $\tilde{\rho}$ in Eqs. (6-8) is not self-consistent with the wavefunction solutions of the corresponding single-particle equation (7), i.e., $\tilde{\rho} \neq \sum_{i=1}^{occ} |\varphi_i|^2$. We return to this issue below.

Since the second term in equation (6) is a smooth quantity, Eq. (2) states that all shell corrections are, to first order in $\delta\rho$, contained in the sum of the single-particle energies $\sum_{i=1}^{occ} \tilde{\varepsilon}_i$. Consequently, equation (6) can be used as a basis for a separation of the total energy into smooth and shell-correction terms as in Eq. (1). Indeed Strutinsky suggested a semi-empirical method of such separation through an averaging procedure of the single-particle energies $\tilde{\varepsilon}_i$ in conjunction with a phenomenological (or semi-empirical) model [the liquid drop model (LDM)] for the smooth part (see section 3).

Motivated by the above considerations, we have extended them ([4]-[6]) in the context of local-density functional theory for electronic structure calculations. First we review pertinent aspects of the LDA theory. In LDA, the total energy is given by

$$E[\rho] = T[\rho] + \int \left\{ \left[\frac{1}{2} V_H[\rho(\mathbf{r})] + V_I(\mathbf{r}) \right] \rho(\mathbf{r}) \right\} d\mathbf{r} + \int \mathcal{E}_{xc}[\rho(\mathbf{r})] d\mathbf{r} + E_I \ , \quad (9)$$

where V_H is the Hartree repulsive potential among the electrons, V_I is the interaction potential between the electrons and ions, $\mathcal{E}_{xc}$ is the exchange-correlation functional [the corresponding xc potential is given as $V_{xc}(\mathbf{r}) \equiv \delta\mathcal{E}_{xc}\rho(\mathbf{r})/\delta\rho(\mathbf{r})$] and $T[\rho]$ is given in terms of a yet unknown functional $t[\rho(\mathbf{r})]$ as $T[\rho] = \int t[\rho(\mathbf{r})] d\mathbf{r}$. E_I is the interaction energy of the ions.

In the Kohn-Sham (KS)-LDA theory, the electron density is evaluated from the single-particle wave functions $\phi_{KS,i}(\mathbf{r})$ as

$$\rho_{KS}(\mathbf{r}) = \sum_{i=1}^{occ} |\phi_{KS,i}(\mathbf{r})|^2 \ , \qquad (10)$$

where $\phi_{KS,i}(\mathbf{r})$ are obtained from a self-consistent solution of the KS equations,

$$\left[-\frac{\hbar^2}{2m} \nabla^2 + V_{KS} \right] \phi_{KS,i}(\mathbf{r}) = \varepsilon_{KS,i} \phi_{KS,i}(\mathbf{r}) \qquad (11)$$

where

$$V_{KS}[\rho_{KS}(\mathbf{r})] = V_H[\rho_{KS}(\mathbf{r})] + V_{xc}[\rho_{KS}(\mathbf{r})] + V_I(\mathbf{r}) \; . \tag{12}$$

The kinetic energy term in Eq. (9) is given by

$$T[\rho_{KS}] = \sum_{i=1}^{occ} < \phi_{KS,i}| - \frac{\hbar^2}{2m}\nabla^2|\phi_{KS,i} > \; , \tag{13}$$

which can also be written as

$$T[\rho_{KS}] = \sum_{i=1}^{occ} \varepsilon_{KS,i} - \int \rho_{KS}(\mathbf{r}) V_{KS}[\rho_{KS}(\mathbf{r})] d\mathbf{r} \; . \tag{14}$$

According to the Hohenberg-Kohn theorem, the energy functional (9) is a minimum at the true ground density ρ_{gs}, which in the context of the KS-LDA theory corresponds the the density, ρ_{KS}, obtained from an iterative self-consistent solution of Eq. (11). In other words, combining Eqs. (9) and (14), and denoting by "in" and "out" the trial and output densities of an iteration cycle in the solution of the KS equations (11), one obtains,

$$\begin{aligned} E_{KS}[\rho_{KS}^{out}] \;\; = \;\; & E_I + \sum_{i=1}^{occ} \varepsilon_{KS,i}^{out} + \\ & \int \left\{ \frac{1}{2} V_H[\rho_{KS}^{out}(\mathbf{r})] + \mathcal{E}_{xc}[\rho_{KS}^{out}(\mathbf{r})] + V_I(\mathbf{r}) \right\} \rho_{KS}^{out}(\mathbf{r}) d\mathbf{r} - \\ & \int \rho_{KS}^{out}(\mathbf{r}) V_{KS}[\rho_{KS}^{in}(\mathbf{r})] d\mathbf{r} \; . \end{aligned} \tag{15}$$

Note that the expression on the right involves both ρ_{KS}^{out} and ρ_{KS}^{in}. Self-consistency is achieved when $\delta\rho_{KS}^{out,in}(\mathbf{r}) = \rho_{KS}^{out}(\mathbf{r}) - \rho_{KS}^{in}(\mathbf{r})$ becomes arbitrarily small (i.e., when ρ_{KS}^{out} converges to ρ_{KS}).

On the other hand, it is desirable to introduce approximate energy functionals for the calculations of ground-state electronic properties, providing simplified, yet accurate, computational schemes. It is indeed possible to construct such functionals ([34]-[38]), an example of which was derived by Harris [34], where self-consistency is circumvented and the result is accurate to second order in the difference between the trial and the self-consistent KS density (see in particular Eq. (24a) of Ref. [38]; the same also holds true for the difference between the trial and the output densities of the Harris functional).

The expression of the Harris functional is obtained from Eq. (15) by dropping the label KS and by replacing everywhere ρ^{out} by ρ^{in}, yielding

[note cancellations between the third and fourth terms on the right-hand-side of Eq. (15)].

$$E_{harris}[\rho^{in}] = E_I + \sum_{i=1}^{occ} \varepsilon_i^{out} - \int \left\{ \frac{1}{2} V_H[\rho^{in}(\mathbf{r})] + V_{xc}[\rho^{in}(\mathbf{r})] \right\} \rho^{in}(\mathbf{r}) d\mathbf{r} + \int \mathcal{E}_{xc}[\rho^{in}(\mathbf{r})] d\mathbf{r} \, . \tag{16}$$

ε_i^{out} are the single-particle solutions (non-self-consistent) of Eq. (11), with $V_{KS}[\rho^{in}(\mathbf{r})$ [see Eq. (12)].

As stated above this result is accurate to second order in $\rho^{in} - \rho_{KS}$ (alternatively in $\rho^{in} - \rho^{out}$), thus approximating the self-consistent total energy $E_{KS}[\rho_{KS}]$.

Obviously the accuracy of the results obtained via Eq. (16) depend on the choice of the input density ρ^{in}. In electronic structure calculations where the corpuscular nature of the ions is included (i.e., all-electron or pseudo-potential calculations), a natural choice for ρ^{in} consists of a superposition of atomic site densities, as suggested originally by Harris. In the case of jellium calculations, we have shown [4] that an accurate approximation to the KS-LDA total energy is obtained by using the Harris functional with the input density, ρ^{in}, in Eq. (16) evaluated from an Extended-Thomas-Fermi (ETF)-LDA calculation.

The ETF-LDA energy functional, $E_{ETF}[\rho]$, is obtained by replacing the kinetic energy term in Eq. (9) by a kinetic energy density-functional in the spirit of the Thomas-Fermi approach [39], but comprising terms up to fourth-order in the density gradients [40]. The optimal ETF-LDA total energy is then obtained by minimization of $E_{ETF}[\rho]$ with respect to the density. In our calculations, we use for the trial densities parametrized profiles $\rho(\mathbf{r}; \{\gamma_i\})$ with $\{\gamma_i\}$ as variational parameters (the ETF-LDA optimal density is denoted as ρ_{ETF}). The single-particle eigenvalues, $\{\varepsilon_i^{out}\}$, in Eq. (16) are obtained then as the solutions to a single-particle Hamiltonian,

$$\hat{H}_{ETF} = -\frac{\hbar^2}{2m} \nabla^2 + V_{ETF} \, , \tag{17}$$

where V_{ETF} is given by Eq. (12) with $\rho_{KS}(\mathbf{r})$ replaced by $\rho_{ETF}(\mathbf{r})$. These single-particle eigenvalues will be denoted by $\{\tilde{\varepsilon}_i\}$

As is well known, the ETF-LDA does not contain shell effects ([20]-[22]). Consequently, the corresponding density ρ_{ETF} can be taken à la Strutinsky as the smooth part, $\tilde{\rho}$, of the KS density, ρ_{KS}. Accordingly, E_{ETF} is identified with the smooth part $\tilde{E}$ in Eq. (1) (in the following,

the "ETF" subscript and " ~ " can be used interchangeably). Since, as aforementioned, $E_{harris}[\rho_{ETF}]$ approximates well [i.e., to second order in $(\rho_{ETF} - \rho_{KS})$] the self-consistent total energy $E_{KS}[\rho_{KS}]$, it follows from Eq. (1), with $E_{harris}[\rho_{ETF}]$ taken as the expression for E_{total}, that the shell-correction, ΔE_{sh}, is given by

$$\Delta E_{sh} = E_{harris}[\rho_{ETF}] - E_{ETF}[\rho_{ETF}] \equiv E_{sh}[\widetilde{\rho}] - \widetilde{E}[\widetilde{\rho}] \; . \tag{18}$$

Defining,

$$T_{sh} = \sum_{i=1}^{occ} \widetilde{\varepsilon}_i - \int \rho_{ETF}(\mathbf{r}) V_{ETF}(\mathbf{r}) d\mathbf{r} \; , \tag{19}$$

and denoting the total energy E_{harris} by E_{sh}, we obtain,

$$E_{sh}[\widetilde{\rho}] = \{T_{sh} - \widetilde{T}[\widetilde{\rho}]\} + \widetilde{E}[\widetilde{\rho}] \; , \tag{20}$$

where $\widetilde{T}[\widetilde{\rho}]$ is the ETF kinetic energy, given to fourth-order gradients by the expression [40],

$$\begin{aligned} T_{ETF}[\rho] \;=\; & \frac{\hbar^2}{2m} \int \left\{ \frac{3}{5}(3\pi^2)^{2/3}\rho^{5/3} + \frac{1}{36}\frac{(\nabla\rho)^2}{\rho} + \frac{1}{270}(3\pi^2)^{-2/3}\rho^{1/3} \right. \\ & \left. \times \left[\frac{1}{3}\left(\frac{\nabla\rho}{\rho}\right)^4 - \frac{9}{8}\left(\frac{\nabla\rho}{\rho}\right)^2 \frac{\Delta\rho}{\rho} + \left(\frac{\Delta\rho}{\rho}\right)^2 \right] \right\} d\mathbf{r} \; , \end{aligned} \tag{21}$$

which as noted before does not contain shell effects. Therefore, the shell correction term in Eq. (1) [or Eq. (18)] is given by a difference between kinetic energy terms,

$$\Delta E_{sh} = T_{sh} - \widetilde{T}[\widetilde{\rho}] \; . \tag{22}$$

One should note that the above derivation of the shell correction does not involve a Strutinsky averaging procedure of the kinetic energy operator. Rather it is based on using ETF quantities as the smooth part for the density, $\widetilde{\rho}$, and energy, $\widetilde{E}$. Other descriptions of the smooth part may result in different shell-correction terms.

To check the accuracy of this procedure, we have compared results of calculations using the functional E_{sh} [Eq. (20)] with available Kohn-Sham calculations. In these SCM calculations, the trial density profile in the ETF variation was chosen as,

$$\rho(r) = \frac{\rho_0}{\left[1 + \exp\left(\frac{r - r_0}{\alpha}\right)\right]^\gamma} \; , \tag{23}$$

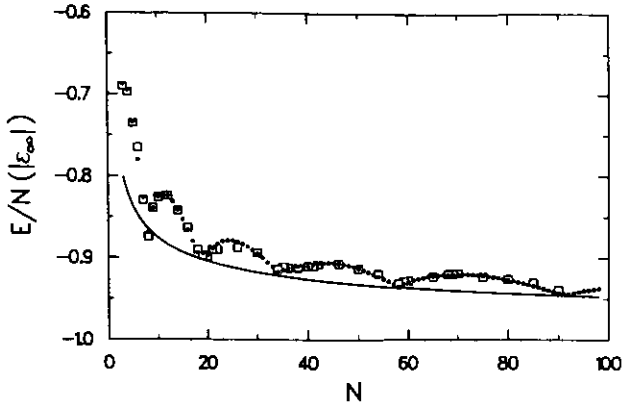

Fig. 2. Total energy per atom of neutral sodium clusters (in units of the absolute value of the energy per atom in the bulk, $|\varepsilon_\infty| = 2.252\ eV$). Solid circles: SCM results (see text for details). The solid line is the ETF result (smooth contribution). In both cases, a spherical jellium background was used. Open squares: LDA Kohn-Sham results from Ref. [41]. The excellent agreement (a discrepancy of only 1%) between the SCM and the LDA Kohn-Sham approach is to be stressed.

with r_0, α, and γ as variational parameters (for other closely related parametrizations cf. Refs. [21, 22]).

Fig. 2 displays results of the present shell correction approach for the total energies of neutral sodium clusters. The results of the shell correction method for ionization potentials of sodium clusters are displayed in Fig. 3. The excellent agreement between the oscillating results obtained via our theory and the Kohn-Sham results (cf. e.g., Ref. [41]) is evident. To further illustrate the two components (smooth contribution and shell correction) entering into our approach, we also display the smooth parts resulting from the ETF method.

2.2 Applications of LDA-SCM

2.2.1 Charging of metal clusters

Investigations of metal clusters based on LDA methods and self-consistent solutions of the Kohn-Sham equations (employing either a positive jellium background or maintaining the discrete ionic cores) have contributed significantly to our understanding of these systems ([41]-[44]). However, even for singly negatively charged metal clusters (M_N^-), difficulties may arise due to the failure of the solutions of the KS equations to converge, since the eigenvalue of the excess electron may iterate to a positive energy [45]. While such

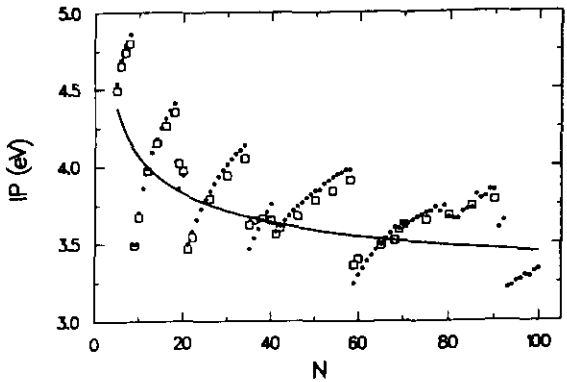

Fig. 3. Ionization potentials for sodium clusters. Solid circles: IPs calculated with the SCM (see text for details). The solid line corresponds to the ETF results (smooth contribution). In both cases, a spherical jellium background was used. Open squares: LDA Kohn-Sham results from Ref. [41]. The excellent agreement (a discrepancy of only 1-2%) between the shell correction method and the full Kohn-Sham approach should be noted.

difficulties are alleviated for M_N^- clusters via self-interaction corrections (SIC) [46, 47], the treatment of multiply charged clusters (M_N^{Z-}, $Z > 1$) would face similar difficulties in the metastability region against electronic autodetachment through a Coulombic barrier. In the following we are applying our SCM approach, described in the previous section, to these systems ([4]-[6]) (for the jellium background, we assume spherical symmetry, unless otherwise stated; for a discussion of cluster deformations, see section 3.2).

Electron affinities and borders of stability

The smooth multiple electron affinities $\tilde{A}_Z$ prior to shell corrections are defined as the difference in the total energies of the clusters

$$\tilde{A}_Z = \tilde{E}(vN, vN + Z - 1) - \tilde{E}(vN, vN + Z)\,, \tag{24}$$

where N is the number of atoms, v is the valency and Z is the number of excess electrons in the cluster (e.g., first and second affinities correspond to $Z = 1$ and $Z = 2$, respectively). vN is the total charge of the positive background. Applying the shell correction (22), we calculate the full electron affinity as

$$A_Z^{sh} - \tilde{A}_Z = \Delta E_{sh}(vN, vN + Z - 1) - \Delta E_{sh}(vN, vN + Z)\,. \tag{25}$$

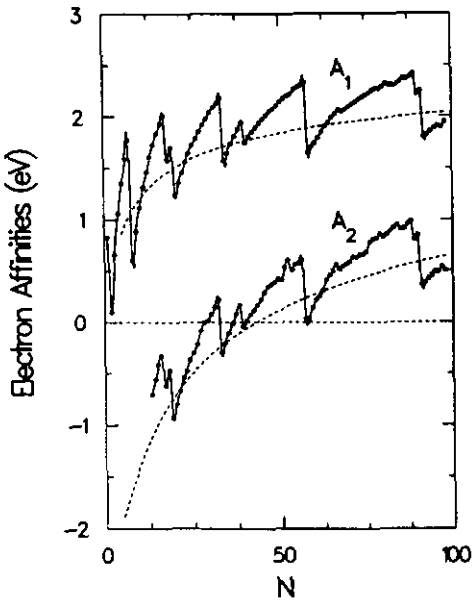

Fig. 4. Calculated first (A_1) and second (A_2) electron affinities of sodium clusters as a function of the number of atoms N. Both their smooth part (dashed lines) and the shell-corrected affinities (solid circles) are shown. A spherical jellium background was used.

A positive value of the electron affinity indicates stability upon attachment of an extra electron. Fig. 4 displays the smooth, as well as the shell corrected, first and second electron affinities for sodium clusters with $N < 100$. Note that $\tilde{A}_2$ becomes positive above a certain critical size, implying that the second electron in doubly negatively charged sodium clusters with $N < N_{\rm cr}^{(2)} = 43$ might not be stably attached. The shell effects, however, create two islands of stability about the magic clusters Na_{32}^{2-} and Na_{38}^{2-} (see A_2^{sh} in Fig. 4). To predict the critical cluster size $N_{\rm cr}^{(Z)}$, which allows stable attachment of Z excess electrons, we calculated the smooth electron affinities of sodium clusters up to $N = 255$ for $1 \leq Z \leq 4$, and display the results in Fig. 5. We observe that $N_{\rm cr}^{(3)} = 205$, while $N_{\rm cr}^{(4)} > 255$.

The similarity of the shapes of the curves in Fig. 5, and the regularity of distances between them, suggest that the smooth electron affinities can be fitted by a general expression of the form:

$$\tilde{A}_Z = \tilde{A}_1 - \frac{(Z-1)e^2}{R+\delta} = W - \beta\frac{e^2}{R+\delta} - \frac{(Z-1)e^2}{R+\delta}, \qquad (26)$$

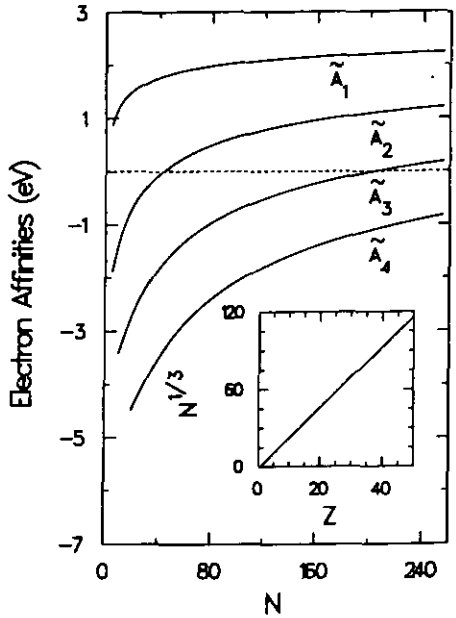

Fig. 5. Calculated smooth electron affinities $\tilde{A}_Z$, Z = 1-4, for sodium clusters as a function of the number of atoms N (Z is the number of excess electrons). A spherical jellium background was used. Inset: The electron *drip* line for sodium clusters. Clusters stable against spontaneous electron emission are located above this line. While, as seen from Fig. 4 for spherical geometry, shell effects influence the border of stability, shell-corrected calculations including deformations [7] yield values close to the drip line (shown in the inset) which was obtained from the smooth contributions.

where the radius of the positive background is $R = r_s N^{1/3}$. From our fit, we find that the constant W corresponds to the bulk work function. In all cases, we find $\beta = 5/8$, which suggests a close analogy with the classical model of the image charge [48, 49]. For the spill-out parameter, we find a weak size dependence as $\delta = \delta_0 + \delta_2/R^2$. The contribution of δ_2/R^2, which depends on Z, is of importance only for smaller sizes and does not affect substantially the critical sizes (where the curve crosses the zero line), and consequently δ_2 can be neglected in such estimations. Using the values obtained by us for $\tilde{A}_1$ of sodium clusters (namely, $W = 2.9\ eV$ which is also the value obtained by KS-LDA calculations for an infinite planar surface [50], $\delta_0 = 1.16\ a.u.$; with $R = r_s N^{1/3}$, and $r_s = 4.00\ a.u.$), we find for the critical sizes when the l.h.s. of eq. (26) is set equal to zero, $N_{\rm cr}^{(2)} = 44$, $N_{\rm cr}^{(3)} = 202$, $N_{\rm cr}^{(4)} = 554$, and $N_{\rm cr}^{(5)} = 1177$, in very good agreement with

the values obtained directly from Fig. 5.

The curve that specifies $N_{cr}^{(Z)}$ in the (Z, N) plane defines the border of stability for spontaneous electron decay. In nuclei, such borders of stability against spontaneous proton or neutron emission are known as nucleon drip lines [51]. For the case of sodium clusters, the electron drip line is displayed in the inset of Fig. 5.

Critical sizes for potassium and aluminum

While in this investigation we have used sodium clusters as a test system, the methodology and conclusions extend to other materials as well. Thus given a calculated or measured bulk work function W, and a spill-out parameter (δ_0 typically of the order of 1-2 *a.u.*, and neglecting δ_2), one can use eq. (26), with $\tilde{A}_Z = 0$, to predict critical sizes for other materials. For example, our calculations for potassium ($r_s = 4.86$ *a.u.*) give fitted values $W = 2.6$ *eV* (compared to a KS-LDA value of 2.54 *eV* for a semi-infinite planar surface with $r_s = 5.0$ *a.u.* [50]) and $\delta_0 = 1.51$ *a.u.* for $\delta_2 = 0$, yielding $N_{cr}^{(2)} = 33$, $N_{cr}^{(3)} = 152$, and $N_{cr}^{(4)} = 421$.

As a further example, we give our results for a trivalent metal, i.e. aluminum ($r_s = 2.07$ *a.u.*), for which our fitted values are $W = 3.65$ *eV* (compared to a KS-LDA value of 3.78 *eV* for a semi-infinite plane surface, with $r_s = 2.0$ *a.u.* [50]) and $\delta_0 = 1.86$ *a.u.* for $\delta_2 = 0$, yielding $N_{cr}^{(2)} = 40$ (121 electrons), $N_{cr}^{(3)} = 208$ (626 electrons), and $N_{cr}^{(4)} = 599$ (1796 electrons).

Metastability against electron autodetachment

The multiply charged anions with negative affinities do not necessarily exhibit a positive total energy. To illustrate this point, we display in Fig. 6 the calculated total energies per atom ($\tilde{E}(N, Z)/N$) as a function of excess charge (Z) for clusters containing 30, 80, and 240 sodium atoms. These sizes allow for exothermic attachment of maximum one, two, or three excess electrons, respectively.

As was the case with the electron affinities, the total-energy curves in Fig. 6 show a remarkable regularity, suggesting a parabolic dependence on the excess charge. To test this conjecture, we have extracted from the calculated total energies the quantity $g(N, Z) = G(N, Z)/N$ where $G(N, Z) = [\tilde{E}(N, Z) - \tilde{E}(N, 0)]/Z + \tilde{A}_1(N)$, and have plotted it in the inset of Fig. 6 as a function of the excess negative charge Z. The dependence is

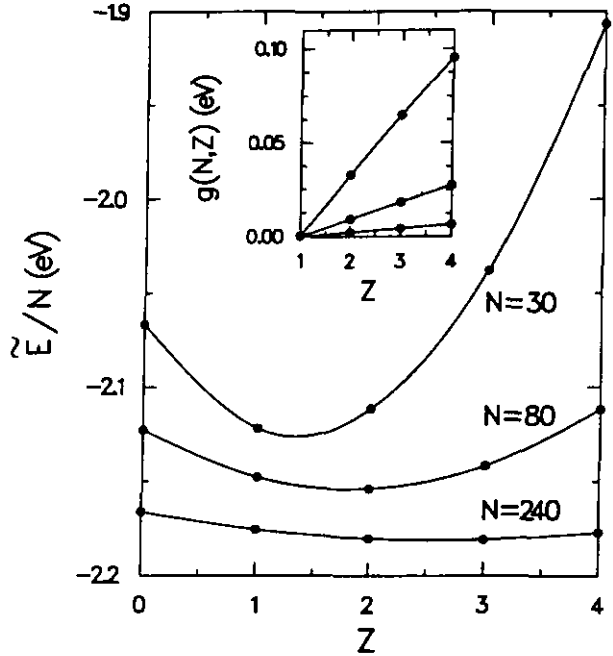

Fig. 6. Calculated *smooth* total energy per atom as a function of the excess negative charge Z for the three families of sodium clusters with $N = 30$, $N = 80$, and $N = 240$ atoms. A spherical jellium background was used. As the straight lines in the inset demonstrate, the curves are parabolic. We find that they can be fitted by eq. (27). See text for an explanation of how the function $g(N, Z)$ was extracted from the calculations.

linear to a remarkable extent; for $Z = 1$ all three lines cross the energy axis at zero. Combined with the results on the electron affinities, this indicates that the total energies have the following dependence on the excess number of electrons (Z):

$$\tilde{E}(Z) = \tilde{E}(0) - \tilde{A}_1 Z + \frac{Z(Z-1)e^2}{2(R+\delta)}, \tag{27}$$

where the dependence on the number of atoms in the cluster is not explicitly indicated.

This result is remarkable in its analogy with the classical image-charge result of van Staveren *et al.* [49]. Indeed, the only difference amounts to the spill-out parameter δ_0 and to the weak dependence on Z through δ_2. This additional Z-dependence becomes negligible already for the case of 30 sodium atoms.

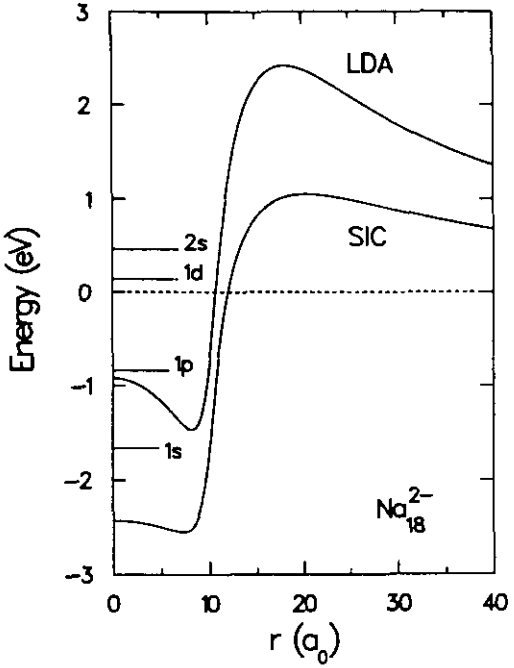

Fig. 7. The LDA and the corresponding self-interaction corrected (SIC) potential for the metastable Na_{18}^{2-} cluster. A spherical jellium background was used. The single-particle levels of the SIC potential are also shown. Unlike the LDA, this latter potential exhibits the correct asymptotic behavior. The $2s$ and $1d$ electrons can be emitted spontaneously by tunneling through the Coulombic barrier of the SIC potential. Distances in units of the Bohr radius, a_0.

For metastable multiply-charged cluster anions, electron emission (autodetachment) will occur via tunneling through a barrier (shown in Fig. 7). However, to reliably estimate the electron emission, it is necessary to correct the LDA effective potential for self-interaction effects. We performed a self-interaction correction of the Amaldi type [45] for the Hartree term and extended it to the exchange-correlation contribution to the total energy as follows: $E_{\rm xc}^{\rm SIC}[\rho] = E_{\rm xc}^{\rm LDA}[\rho] - N_e E_{\rm xc}^{\rm LDA}[\rho/N_e]$, where $N_e = vN + Z$ is the total number of electrons. This self-interaction correction is akin to the orbitally-averaged-potential method [45]. Minimizing the SIC energy functional for the parameters r_0, α, and γ, we obtained the effective SIC potential for Na_{18}^{2-} shown in Fig. 7, which exhibits the physically correct asymptotic behavior [52].

The spontaneous electron emission through the Coulombic barrier is

analogous to that occurring in proton radioactivity from neutron-deficient nuclei [53], as well as in alpha-particle decay. The transition rate is $\lambda = \ln 2/T_{1/2} = \nu P$, where ν is the attempt frequency and P is the transmission coefficient calculated in the WKB method (for details, cf. Ref. [53]). For the $2s$ electron in Na_{18}^{2-} (cf. Fig. 7), we find $\nu = 0.73\ 10^{15}\ Hz$ and $P = 4.36\ 10^{-6}$, yielding $T_{1/2} = 2.18\ 10^{-10}\ s$. For a cluster size closer to the drip line (see Fig. 5), e.g. Na_{35}^{2-}, we find $T_{1/2} = 1.13\ s$.

Finally, exression (27) for the total energy can be naturally extended to the case of multiply *positively* charged metal clusters by setting $Z = -z$, with $z > 0$. The ensuing equatiou retains the same dependence on the excess positive charge z, but with the negative value of the first affinity, $-\widetilde{A}_1$, replaced by the positive value of the first ionization potential, $\widetilde{I}_1 = W + (3/8)e^2/(R + \delta)$, a result that has been suggested from earlier measurements on multiply charged potassium cations [54]. Naturally, the spill-out parameter δ assumes different values than in the case of the anionic clusters.

2.2.2 Neutral and multiply charged fullerenes

Stabilized jellium approximation - The generalized LDA-SCM

Fullerenes and related carbon structures have been extensively investigated using *ab initio* local-density-functional methods and self-consistent solutions of the Kohn-Sham (KS) equations [55, 56]. For metal clusters, replacing the ionic cores with a uniform jellium background was found to describe well their properties within the KS-LDA method [30]. Motivated by these results, several attempts to apply the jellium model in conjunction with LDA to investigations of fullerenes have appeared recently [57, 58, 59, 14]. Our approach [14] differs from the earlier ones in several aspects and, in particular, in the adaptation to the case of finite systems of the stabilized-jellium (or structureless pseudopotential) energy density functional (see eq. (28) below and Ref. [45]).

An important shortcoming of the standard jellium approximation for fullerenes (and other systems with high density , i.e., small r_s) results from a well-known property of the jellium at high electronic densities, namely that the jellium is unstable and yields negative surface-energy contribution to the total energy [45], as well as unreliable values for the total energy. These inadequacies of the standard jellium model can be rectified by pseudopotential corrections. A modified-jellium approach which incorporates such pseudopotential corrections and is particularly suited for our pur-

poses here, is the *structureless pseudopotential* model or *stabilized jellium* approximation developed in Ref. [45].

In the stabilized jellium, the total energy E_{pseudo}, as a functional of the electron density $\rho(\mathbf{r})$, is given by the expression

$$E_{pseudo}[\rho,\rho_+] = E_{jell}[\rho,\rho_+] + \langle \delta v \rangle_{WS} \int \rho(\mathbf{r})\mathcal{U}(\mathbf{r})d\mathbf{r} - \widetilde{\varepsilon} \int \rho_+(\mathbf{r})d\mathbf{r} \ , \quad (28)$$

where by definition the function $\mathcal{U}(\mathbf{r})$ equals unity inside, but vanishes, outside the jellium volume. ρ_+ is the density of the positive jellium background (which for the case of C_{60} is taken as a spherical shell, of a certain width $2d$, centered at 6.7 *a.u.*). E_{pseudo} in eq. (28) is the standard jellium-model total energy, E_{jell}, modified by two corrections. The first correction adds the effect of an average (i.e., averaged over the volume of a Wigner-Seitz cell) difference potential, $\langle \delta v \rangle_{WS}\mathcal{U}(\mathbf{r})$, which acts on the electrons in addition to the standard jellium attraction and is due to the atomic pseudopotentials (in this work, we use the Ashcroft empty-core pseudopotential, specified by a core radius r_c, as in Ref. [45]). The second correction subtracts from the jellium energy functional the spurious electrostatic self-repulsion of the positive background within each cell; this term makes no contribution to the effective electronic potential.

Following Ref. [45], the bulk stability condition (eq. (25) in Ref. [45]) determines the value of the pseudopotential core radius r_c, as a function of the bulk Wigner-Seitz radius r_s. Consequeutly, the difference potential can be expressed solely as a function of r_s as follows (energies in *Ry*, distances in *a.u.*):

$$\langle \delta v \rangle_{WS} = -\frac{2}{5}\left(\frac{9\pi}{4}\right)^{2/3} r_s^{-2} + \frac{1}{2\pi}\left(\frac{9\pi}{4}\right)^{1/3} r_s^{-1} + \frac{1}{3} r_s \frac{d\varepsilon_c}{dr_s} \ , \quad (29)$$

where ε_c is the per particle electron-gas correlation energy (in our calculation, we use the Gunnarsson-Lundqvist exchange and correlation energy functionals (see Refs. [4, 5])).

The electrostatic self-energy, $\widetilde{\varepsilon}$, per unit charge of the uniform positive jellium is given by

$$\widetilde{\varepsilon} = 6v^{2/3}/5r_s \ , \quad (30)$$

where v is the valence of the atoms ($v = 4$ for carbon).

ETF electron-density profile

To apply the ETF-LDA method to carbon fullerenes, we generalize it by employing potential terms according to the stabilized-jellium functional (28).

Another required generalization consists in employing a parametrized electron-density profile that accounts for the hollow cage-structure of the fullerenes. Such a density profile is provided by the following adaptation of a generalization of an inverse Thomas-Fermi distribution, used earlier in the context of nuclear physics [60], i.e.,

$$\rho(r) = \rho_0 \left(\frac{F_{i,o} \sinh[w_{i,o}/\alpha_{i,o}]}{\cosh[w_{i,o}/\alpha_{i,o}] + \cosh[(r-R)/\alpha_{i,o}]} \right)^{\gamma_{i,o}} , \qquad (31)$$

where $R = 6.7$ *a.u.* is the radius of the fullerene cage. w, α, and γ are variables to be determined by the ETF-LDA minimization. For $R = 0$ and large values of w/α, expression (31) approaches the more familiar inverse Thomas-Fermi distribution, with w the width, α the diffuseness and γ the asymmetry of the profile around $r = w$. There are a total of six parameters to be determined, since the indices (i, o) stand for the regions inside $(r < R)$ and outside $(r > R)$ the fullerene cage. $F_{i,o} = (\cosh[w_{i,o}/\alpha_{i,o}] + 1)/\sinh[w_{i,o}/\alpha_{i,o}]$ is a constant guaranteeing that the two parts of the curve join smoothly at $r = R$. The density profile in Eq. (31) peaks at $r = R$ and then falls towards smaller values both inside and outside the cage (see top panel of Fig. 8).

Shell correction and icosahedral splitting

To apply the SCM to the present case, the potential V_{ETF} in Eq. (19) is replaced by the stabilized-jellium LDA potential shown in Fig. 8. After some rearrangements, the shell-corrected total energy $E_{sh}[\widetilde{\rho}]$ in the stabilized-jellium case can be written in functional form as follows [compare to Eq. (20), see also Eq. (16].

$$E_{sh}[\widetilde{\rho}] = \sum_i \widetilde{\varepsilon}_i \; - \; \int \left\{ \frac{1}{2} \widetilde{V}_H(\mathbf{r}) + \widetilde{V}_{xc}(\mathbf{r}) \right\} \widetilde{\rho}(\mathbf{r}) d\mathbf{r}$$
$$+ \; \int \widetilde{\mathcal{E}}_{xc}[\widetilde{\rho}(\mathbf{r})] d\mathbf{r} + E_I - \widetilde{\varepsilon} \int \rho_+(\mathbf{r}) d\mathbf{r} \; , \qquad (32)$$

Heretofore, the point-group icosahedral symmetry of C_{60} was not considered, since the molecule was treated as a spherically symmetric cage. This is a reasonable zeroth-order approximation as noticed by several authors [55, 59, 61, 62]. However, considerable improvement is achieved when

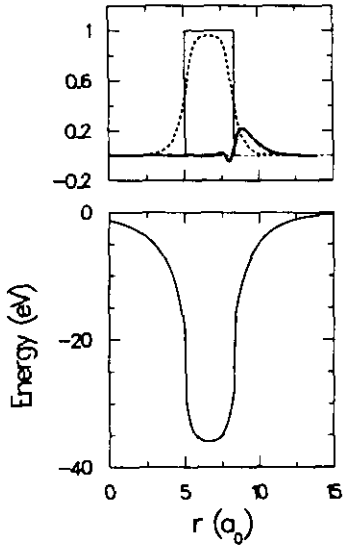

Fig. 8. Bottom panel: The stabilized-jellium LDA potential obtained by the ETF method for the neutral C_{60} molecule. The Wigner-Seitz radius for the jellium bacground is 1.23 *a.u.* Note the asymmetry of the potential about the minimum. The associated difference potential $\langle \delta v \rangle_{WS} = -9.61\ eV$.
Top panel: Solid line: Radial density of the positive jellium background. Dashed line: ETF electronic density. Note its asymmetry about the maximum. Thick solid line: The difference (multiplied by 10) of electronic ETF densities between C_{60}^{5-} and C_{60}. It illustrates that the excess charge accumulates in the outer perimeter of the total electronic density. All densities are normalized to the density of the positive jellium background.

the effects of the point-group icosahedral symmetry are considered as a next-order correction (mainly the lifting of the angular momentum degeneracies).

The method of introducing the icosahedral splittings is that of the crystal field theory [63]. Thus, we will use the fact that the bare electrostatic potential from the ionic cores, considered as point charges, acting upon an electron, obeys the well-known expansion theorem [63]

$$U(\mathbf{r}) = -ve^2 \sum_i \frac{1}{|\mathbf{r} - \mathbf{r}_i|} = -\sum_{l=0}^{\infty} \sum_{m=-l}^{l} \kappa_l(r) C_l^m Y_l^m(\theta, \phi)\ , \qquad (33)$$

where the angular coefficients C_l^m are given through the angular coordinates

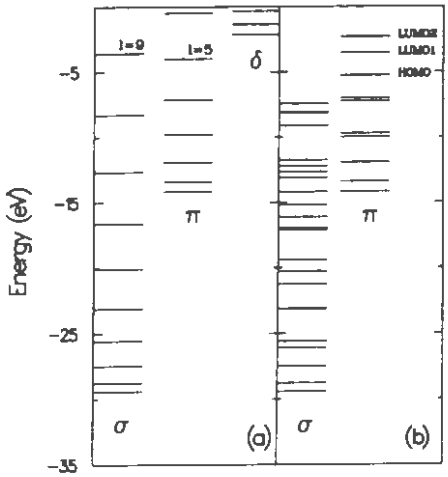

Fig. 9. (a) The single-particle levels of the ETF-LDA potential for C_{60} shown in Fig. 8. Because of the spherical symmetry, they are characterized by the two principle quantum numbers n_r and l, where n_r is the number of radial nodes and l the angular momentum. They are grouped in three bands labeled σ ($n_r = 0$), π ($n_r = 1$), and δ ($n_r = 2$). Each band starts with an $l = 0$ level.
(b) The single-particle levels for C_{60} after the icosahedral splittings are added to the spectra of (a). The tenfold degenerate HOMO (h_u) and the sixfold degenerate LUMO1 (t_{1u}) and LUMO2 (t_{1g}) are denoted; they originate from the spherical $l = 5$ and $l = 6$ (t_{1g}) π levels displayed in panel (a). For the σ electrons, the icosahedral perturbation strongly splits the $l = 9$ level of panel (a). There result five sublevels which straddle the σ-electron gap as follows: two of them (the eightfold degenerate g_u, and the tenfold degenerate h_u) move down and are fully occupied resulting in a shell closure (180 σ electrons in total). The remaining unoccupied levels, originating from the $l = 9$ σ level, are sharply shifted upwards and acquire positive values.

θ_i, ϕ_i of the carbon atomic cores, namely,

$$C_l^m = \sum_i Y_l^{m*}(\theta_i, \phi_i) \ , \tag{34}$$

where $*$ denotes complex conjugation.

We take the radial parameters $\kappa_l(r)$ as constants, and determine their value by adjusting the icosahedral single-particle spectra ε_i^{ico} to reproduce the pseudopotential calculation of Ref. [55], which are in good agreement with experimental data. Our spectra without and with icosahedral splitting are shown in Fig. 9(a) and Fig. 9(b), respectively. We find that a close reproduction of the results of *ab initio* LDA calculations [55, 64, 65] is

achieved when the Wigner-Seitz radius for the jellium background is 1.23 *a.u.* The shell corrections, ΔE_{sh}^{ico}, including the icosahedral splittings are calculated using the icosahedral single-particle energies ε_i^{ico} in eq. (19). The average quantities ($\tilde{\rho}$ and $\tilde{V}$) are maintained as those specified through the ETF variation with the spherically symmetric profile of eq. (31). This is because the first-order correction to the total energy (resulting from the icosahedral perturbation) vanishes, since the integral over the sphere of a spherical harmonic Y_l^m ($l > 0$) vanishes.

Ionization potentials and electron affinities

Having specified the appropriate Wigner-Seitz radius r_s and the parameters κ_l of the icosahedral crystal field through a comparison with the pseudopotential LDA calculations for the neutral C_{60}, we calculate the total energies of the cationic and anionic species by allowing for a change in the total electronic charge, namely by imposing the constraint

$$4\pi \int \rho(r) r^2 dr = 240 \pm x \ , \tag{35}$$

where $\rho(r)$ is given by eq. (31). The shell-corrected and icosahedrally perturbed first and higher ionization potentials I_x^{ico} are defined as the difference of the ground-state shell-corrected total energies E_{sh}^{ico} as follows:

$$I_x^{ico} = E_{sh}^{ico}(N_e = 240-x; Z = 240) - E_{sh}^{ico}(N_e = 240-x+1; Z = 240) \ , \tag{36}$$

where N_e is the number of electrons in the system and x is the number of excess charges on the fullerenes (for the excess charge, we will find convenient to use two different notations x and z related as $x = |z|$. A negative value of z corresponds to positive excess charges). $Z = 240$ denotes the total positive charge of the jellium background.

The shell-corrected and icosahedrally perturbed first and higher electron affinities A_x^{ico} are similarly defined as

$$A_x^{ico} = E_{sh}^{ico}(N_e = 240+x-1; Z = 240) - E_{sh}^{ico}(N_e = 240+x; Z = 240) \ . \tag{37}$$

We have also calculated the corresponding average quantities $\tilde{I}_x$ and $\tilde{A}_x$, which result from the ETF variation with spherical symmetry (that is without shell and icosahedral symmetry corrections). Their definition is the same as in Eqs. (36) and (37), but with the index *sh* replaced by a tilde and the removal of the index *ico*.

Table I. ETF (spherically averaged, denoted by a tilde) and shell-corrected (denoted by a superscript *ico* to indicate that the icosahedral splittings of energy levels have been included) IPs and EAs of fullerenes $C_{60}^{x\pm}$. Energies in eV. $r_s = 1.23$ $a.u.$

x	$\tilde{I}_x$	I_x^{ico}	$\tilde{A}_x$	A_x^{ico}
1	5.00	7.40	2.05	2.75
2	7.98	10.31	−0.86	−0.09
3	10.99	13.28	−3.75	−2.92
4	14.03	16.25	−6.60	−5.70
5	17.09	19.22	−9.41	−8.41
6	20.18	22.20	−12.19	−11.06
7	23.29	25.24	−14.94	−14.85
8	26.42	28.31	−17.64	−17.24
9	29.57	31.30	−20.31	−19.49
10	32.73	34.39	−22.94	−21.39
11	35.92	39.36	−25.53	−22.93
12	39.12	42.51	−28.07	−23.85

In our calculations of the charged fullerene molecule, the r_s value and the icosahedral splitting parameters (κ_l, see Eq. (33), and discussion below it) were taken as those which were determined by our calculations of the neutral molecule, discussed in the previous section. The parameters which specify the ETF electronic density (Eq. (31)) are optimized for the charged molecule, thus allowing for relaxation effects due to the excess charge. This procedure is motivated by results of previous electronic structure calculations for C_{60}^{+} and C_{60}^{-} [64, 65], which showed that the icosahedral spectrum of the neutral C_{60} shifts almost rigidly upon charging of the molecule.

Shell-corrected and ETF calculated values of ionization potentials (IPs) and electron affinities (EAs), for values of the excess charge up to 12 units, are summarized in Table I (for $r_s = 1.23$ $a.u.$)

Charging energies and capacitance of fullerenes

Fig. 10(a) shows that the variation of the total ETF-LDA energy difference (appearance energies) $\Delta\tilde{E}(z) = \tilde{E}(z) - \tilde{E}(0)$, as a function of excess charge z ($|z| = x$), exhibits a parabolic behavior. The inset in Fig. 10(a) exhibiting

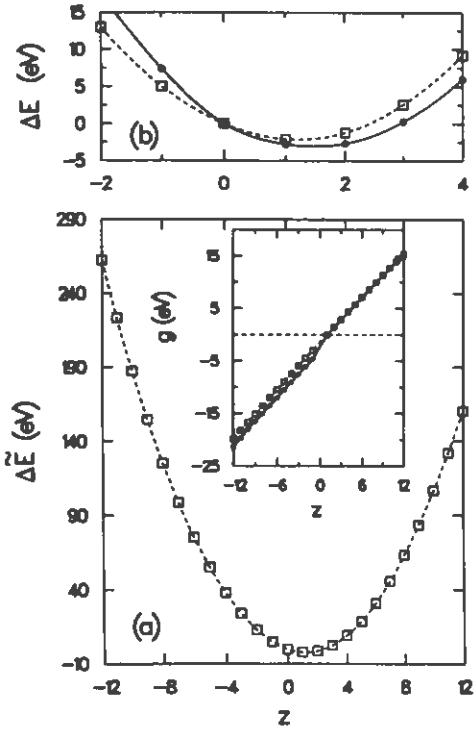

Fig. 10. (a) ETF-LDA total energy differences (appearance energies) $\Delta\widetilde{E}(z) = \widetilde{E}(z) - \widetilde{E}(0)$ as a function of the excess charge z ($z < 0$ corresponds to positive excess charge). Inset: The ETF function $\widetilde{g}(z)$ (open squares), and the shell-corrected function $g_{sh}^{ico}(z)$ (filled circles). For $z \geq 1$ the two functions are almost identical.
(b) magnification of the appearance-energy curves for the region $-2 \leq z \leq 4$. Filled circles: shell-corrected icosahedral values $[\Delta E_{sh}^{ico}(z) = E_{sh}^{ico}(z) - E_{sh}^{ico}(0)]$. Open squares: ETF-LDA values $[\Delta\widetilde{E}(z) = \widetilde{E}(z) - \widetilde{E}(0)]$.

the quantity

$$\widetilde{g}(z) = \frac{\widetilde{E}(z) - \widetilde{E}(0)}{z} + \widetilde{A}_1 \ , \tag{38}$$

plotted versus z (open squares), shows a straight line which crosses the zero energy line at $z = 1$. As a result the total ETF-LDA energy has the form,

$$\widetilde{E}(z) = \widetilde{E}(0) + \frac{z(z-1)e^2}{2C} - \widetilde{A}_1 z \ . \tag{39}$$

Equation (39) indicates that fullerenes behave on the average like a capacitor having a capacitance C (the second term on the rhs of eq. (39)

corresponds to the charging energy of a classical capacitor, corrected for the self-interaction of the excess charge [4, 5]). We remark that regarding the system as a classical conductor, where the excess charge accumulates on the outer surface, yields a value of $C = 8.32\ a.u.$ (that is the outer radius of the jellium shell). Naturally, the ETF calculated value for C is somewhat larger because of the quantal spill-out of the electronic charge density. Indeed, from the slope of $\tilde{g}(z)$ we determine [66] $C = 8.84\ a.u.$

A similar plot of the shell-corrected and icosahedrally modified energy differences $\Delta E^{ico}_{sh}(z) = E^{ico}_{sh}(z) - E^{ico}_{sh}(0)$ is shown in Fig. 10(b) (in the range $-2 \le z \le 4$, filled circles). The function $g^{ico}_{sh}(z)$, defined as in eq. (38) but with the shell-corrected quantities ($\Delta E^{ico}_{sh}(z)$ and A^{ico}_1), is included in the inset to Fig. 10(a) (filled circles). The shift discernible between $g^{ico}_{sh}(-1)$ and $g^{ico}_{sh}(1)$ is approximately $1.7\ eV$, and originates from the difference of shell effects on the IPs and EAs (see Table I). The segments of the curve $g^{ico}_{sh}(z)$ in the inset of Fig. 10(a), corresponding to positively ($z < 0$) and negatively ($z > 0$) charged states, are again well approximated by straight lines, whose slope is close to that found for $\tilde{g}(z)$. Consequently, we may approximate the charging energy, including shell-effects, as follows,

$$E^{ico}_{sh}(x) = E^{ico}_{sh}(0) + \frac{x(x-1)e^2}{2C} - A^{ico}_1 x\ , \tag{40}$$

for *negatively* charged states, and

$$E^{ico}_{sh}(x) = E^{ico}_{sh}(0) + \frac{x(x-1)e^2}{2C} + I^{ico}_1 x\ , \tag{41}$$

for *positively* charged states. Note that without shell-corrections (i.e., ETF) $\tilde{I}_1 - \tilde{A}_1 = e^2/C = 27.2/8.84\ eV \approx 3.1\ eV$, because of the symmetry of eq. (39) with respect to z, while the shell-corrected quantities are related as $I^{ico}_1 - A^{ico}_1 \approx e^2/C + \Delta_{sh}$, where the shell correction is $\Delta_{sh} \approx 1.55\ eV$ (from Table I, $I^{ico}_1 - A^{ico}_1 \approx 4.65\ eV$).

Expression (40) for the negatively charged states can be rearranged as follows (energies in units of eV),

$$E^{ico}_{sh}(x) - E^{ico}_{sh}(0) = -2.99 + 1.54(x - 1.39)^2\ , \tag{42}$$

in close agreement with the all-electron LDA result of Ref. [67].

Equations (40) and (41) can be used to provide simple analytical approximations for the higher IPs and EAs. Explicitly written, $A^{ico}_x \equiv E^{ico}_{sh}(x-1) - E^{ico}_{sh}(x) = A^{ico}_1 - (x-1)e^2/C$ and $I^{ico}_x = I^{ico}_1 + (x-1)e^2/C$. Such expressions have been used previously [68] with an assumed value for $C \approx 6.7\ a.u.$

(i.e., the radius of the C_{60} molecule, as determined by the distance of carbon nuclei from the center of the molecule), which is appreciably smaller than the value obtained by us ($C = 8.84$ *a.u.*, see above) via a microscopic calculation. Consequently, using the above expression with our calculated value for $A_1^{ico} = 2.75$ *eV* (see Table I), we obtain an approximate value of $A_2^{ico} = -0.35$ *eV* (compared to the microscopically calculated value of -0.09 *eV* given in Table I, and -0.11 *eV* obtained by Ref. [67]) — indicating metastability of C_{60}^{2-} — while employing an experimental value for $A_1^{ico} = 2.74$ *eV*, a value of $A_2^{ico} = 0.68$ *eV* was calculated in Ref. [68].

Concerning the cations, our expression (41) with a calculated $I_1^{ico} = 7.40$ *eV* (see Table I) and $C = 8.84$ *a.u.* yields approximate values 18.5 *eV* and 31.5 *eV* for the appearance energies of C_{60}^{2+} and C_{60}^{3+} (compared to the microscopic calculated values of 17.71 *eV* and 30.99 *eV*, respectively, extracted from Table I, and 18.6 *eV* for the former obtained in Ref. [64]). Employing an experimental value for $I_1^{ico} = 7.54$ *eV*, corresponding values of 19.20 *eV* and 34.96 *eV* were calculated in Ref. [68]. As discussed in Ref. [69], these last values are rather high, and the origin of the discrepancy may be traced to the small value of the capacitance which was used in obtaining these estimates in Ref. [68].

A negative value of the second affinity indicates that C_{60}^{2-} is unstable against electron autodetachment. In this context, we note that the doubly negatively charged molecule C_{60}^{2-} has been observed in the gas phase and is believed to be a long-lived metastable species [70, 71]. Indeed, as we discuss in the next section, the small LDA values of A_2^{ico} found by us and by Ref. [67] yield lifetimes which are much longer than those estimated by a pseudopotential-like Hartree-Fock model calculation [70], where a value of ~ 1 μs was estimated.

Lifetimes of metastable anions, C_{60}^{x-}

The second and higher electron affinities of C_{60} were found to be negative, which implies that the anions C_{60}^{x-} with $x \geq 2$ are not stable species, and can lower their energy by emitting an electron. However, unless the number of excess electrons is large enough, the emission of an excess electron involves tunneling through a barrier. Consequently, the moderately charged anionic fullerenes can be described as metastable species possessing a decay lifetime.

To calculate the lifetime for electron autodetachmant, it is necessary to determine the proper potential that the emitted electron sees as it leaves the molecule. The process is analogous to alpha-particle radioactivity of

atomic nuclei. The emitted electron will have a final kinetic energy equal to the negative of the corresponding higher EA. We estimate the lifetime of the decay process by using the WKB method, in the spirit of the theory of alpha-particle radioactivity, which has established that the main factor in estimating lifetimes is the relation of the kinetic energy of the emitted particle to the Coulombic tail, and not the details of the many-body problem in the immediate vicinity of the parent nucleus.

Essential in this approach is the determination of an appropriate single-particle potential that describes the transmission barrier. It is well known that the LDA potential posseses the wrong tail, since it allows for the electron to spuriously interact with itself. A more appropriate potential would be one produced by the Self-Interaction Correction (SIC) method of Ref. [50]. This potential has the correct Coulombic tail, but in the case of the fullerenes presents another drawback, namely Koopman's theorem is not satisfied to an extent adequate for calculating lifetimes [72]. In this context, we note that Koopman's theorem is known to be poorly satisfied for the case of fullerenes even in Hartree-Fock calculations [73]. Therefore, the HOMO corresponding to the emitted electron, calculated as described above, cannot be used in the WKB tunneling calculation.

Since the final energy of the ejected electron equals the negative of the value of the electron affinity, we seek a potential that, together with the icosahedral perturbation, yields a HOMO level in C_{60}^{x-} with energy $-A_x^{ico}$. We construct this potential through a self-interaction correction to the LDA potential as follows,

$$V_{WKB} = V_{LDA}[\tilde{\rho}] - V_H[\frac{\tilde{\rho}}{N_e}] - V_{xc}[\xi\frac{\tilde{\rho}}{N_e}] \,, \tag{43}$$

where the parameter ξ is adjusted so that the HOMO level of C_{60}^{x-} equals $-A_x^{ico}$. In the above expression, the second term on the rhs is an average self-interaction Hartree correction which ensures a proper long-range behavior of the potential (i.e., correct Coulomb tail), and the third term is a correction to the short-range exchange-correlation.

For the cases of C_{60}^{2-} and C_{60}^{3-} such potentials are plotted in Fig. 11. We observe that they have the correct Coulombic tail, namely a tail corresponding to one electron for C_{60}^{2-} and to two electrons for C_{60}^{3-}. The actual barrier, however, through which the electron tunnels is the sum of the Coulombic barrier plus the contribution of the centrifugal barrier. As seen from Fig. 11, the latter is significant, since the HOMO in the fullerenes possesses a rather high angular momentum ($l = 5$), while being confined in a small volume.

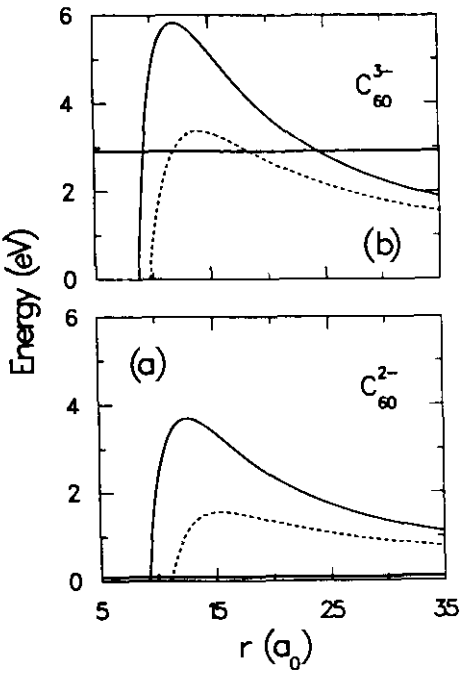

Fig. 11. WKB effective barriers used to estimate lifetimes for C_{60}^{2-} (a) and C_{60}^{3-} (b). Dashed lines correspond to barriers due solely to Coulombic repulsion and solid lines to total barriers after adding the centrifugal components. The thick horizontal solid lines correspond to the negative of the associated electron affinities A_2^{1co} (a) and A_3^{1co} (b). In the case of C_{60}^{2-} [panel (a)], the horizontal solid line at $-A_2^{1co} = 0.09\ eV$ crosses the total barrier at an inside point $R_1 = 9.3\ a.u.$ and again at a distance very far from the center of the fullerene molecule, namely at an outer point $R_2 = -e^2/A_2^{1co} = 27.2/0.09\ a.u. = 302.2\ a.u.$ This large value of R_2, combined with the large centrifugal barrier, yields a macroscopic lifetime for the metastable C_{60}^{2-} (see text for details).

Using the WKB approximation [74], we estimate for C_{60}^{2-} a macroscopic half-life of $\sim 4 \times 10^7$ *years*, while for C_{60}^{3-} we estimate a very short half-life of 2.4×10^{-12} *s*. Both these estimates are in correspondence with observations. Indeed, C_{60}^{3-} has not been observed as a free molecule, while the free C_{60}^{2-} has been observed to be long lived [70, 71] and was detected even 5 *min* after its production through laser vaporization [71].

We note that the WKB lifetimes calculated for tunneling through Coulombic barriers are very sensitive to the final energy of the emitted particle and can vary by many orders of magnitude as a result of small changes in this energy, a feature well known from the alpha radioctivity of nuclei [74]. Since the second electron affinity of C_{60} is small, effects due to geometrical relaxation and spin polarization can influence its value and, consequently, the estimated lifetime. Nevertheless, as shown in Ref. [67], inclusion of such corrections yields again a negative second affinity, but of somewhat smaller magnitude, resulting in an even longer lifetime (the sign conventions in Ref. [67] are the opposite of ours).

Furthermore, as discussed in Ref. [75], the stabilization effect of the Jahn-Teller relaxation for the singly-charged ion is only of the order of 0.03 - 0.05 *eV*. Since this effect is expected to be largest for singly-charged species, C_{60}^{2-} is not expected to be influenced by it [67].

On the other hand, generalized exchange-correlation functionals with gradient corrections yield slightly larger values for the second electron affinity. For example, using exchange-correlation gradient corrections, Ref. [67] found $A_2^{ico} = -0.3$ *eV*, which is higher (in absolute magnitude) than the value obtained without such corrections. This value of -0.3 *eV* leads to a much smaller lifetime than the several million of years that correspond to the value of -0.09 *eV* calculated by us. Indeed, using the barrier displayed in Fig. 11(a), we estimate a lifetime for C_{60}^{2-} of approx. 0.37 *s*, when $A_2^{ico} = -0.3$ *eV*. We stress, however, that even this lower-limit value still corresponds to macroscopic times and is 5 orders of magnitude larger than the estimate of Ref. [70], which found a lifetime of 1 μs for $A_2^{ico} = -0.3$ *eV*, since it omitted the large centrifugal barrier. Indeed, when we omit the centrifugal barrier, we find a lifetime estimate of 1.4 μs, when $A_2^{ico} = -0.3$ *eV*.

3 Semi-empirical shell-correction methods (SE-SCM)

3.1 Methodology

As mentioned above in our introductory description of Strutinsky's work [see section 2.1.2, in particular Eqs. (1-8)], rather than proceed with the microscopic route, he proposed a method for separation of the total energy into smooth and shell-correction terms [see Eq. (1)] based on an averaging procedure. Accordingly, a smooth part, $\widetilde{E}_{sp}$, is extracted out of the sum of the single-particle energies $\sum_i \widetilde{\varepsilon}_i$ [see Eq. (6), or equivalently Eq. (16) with ρ^{in} replaced by $\widetilde{\rho}$ and ε_i^{out} by $\widetilde{\varepsilon}_i$] by averaging them through an appropriate procedure. Usually, but not necessarily, one replaces the delta functions in the single-particle density of states by gaussians or other appropriate weighting functions. As a result, each single-particle level is assigned an averaging occupation number $\widetilde{f}_i$, and the smooth part $\widetilde{E}_{sp}$ is formally written as

$$\widetilde{E}_{sp} = \sum_i \widetilde{\varepsilon}_i \widetilde{f}_i \ . \tag{44}$$

Consequently, the Strutinsky shell correction is given by

$$\Delta E_{sh}^{Str} = \sum_{i=1}^{occ} \widetilde{\varepsilon}_i - \widetilde{E}_{sp} \ . \tag{45}$$

The Strutinsky prescription (45) has the practical advantage of using only the single-particle energies $\widetilde{\varepsilon}_i$, and not the smooth density $\widetilde{\rho}$. Taking advantage of this, the single-particle energies can be taken as those of an external potential that empirically approximates the self-consistent potential of a finite system. In the nuclear case, an anisotropic three-dimensional harmonic oscillator has been used successfully to describe the shell-corrections in deformed nuclei.

The single-particle smooth part, $\widetilde{E}_{sp}$, however, is only one component of the total smooth contribution, $\widetilde{E}[\widetilde{\rho}]$ (E_{HF} in the Hartree-Fock energy considered by Strutinsky). Indeed as can be seen from Eq. (6) [or equivalently Eq. (16)],

$$E_{total} \approx \Delta E_{sh}^{Str} + \widetilde{E}[\widetilde{\rho}] \ . \tag{46}$$

Strutinsky did not address the question of how to calculate microscopically the smooth part $\widetilde{E}$ (which necessarily entails specifying the smooth density $\widetilde{\rho}$). Instead he circumvented this question by substituting for $\widetilde{E}$

the empirical energies, E_{LDM}, of the nuclear liquid drop model, namely he suggested that

$$E_{total} \approx \Delta E_{sh}^{Str} + E_{LDM} \ . \tag{47}$$

In applications of Eq. (47), the single-particle energies involved in the averaging [see Eqs. (44) and (45)] are commonly obtained as solutions of a Schrödinger equation with phenomenological one-body potentials. This last approximation has been very successful in describing fission barriers and properties of strongly deformed nuclei using harmonic oscillator or Wood-Saxon empirical potentials.

In the following, we describe applications of the SE-SCM approach to systematic investigations of the effects of triaxial shape-deformations on the properties of metal clusters [7] (section 3.2.1), and to studies of deformations and barriers in fission of charged metal clusters [8, 9] (section 3.2.2). We mention that, in addition, Strutinsky calculations using phenomenological potentials have been reported for the case of neutral sodium clusters assuming axial symmetry in Refs. ([11]-[13]), and for the case of fission in Ref. [10].

3.2 Applications of the SE-SCM

3.2.1 Electronic shell effects in triaxially deformed metal clusters

Early in the study of alkali-metal clusters, it was recognized that their ground-state properties portray manifestations of electronic shell effects [76, 77, 30, 42]. An important step toward understanding these effects has been achieved by modelling the clusters as spherical jellium droplets, where the ionic structure of the cluster was modeled by a continuous positive charge distribution having a sharp-step spherical profile, and the electrons were treated using density functional theory in the local density approximation [77, 42, 78, 79] (LDA). However, while analyses restricted to consideration of spherical shapes have been able to account for the main discontinuities observed at cluster magic-number sizes (associated with the filling of degenerate levels of valence electronic states which are grouped into a major shell), the results obtained by such spherical models, pertaining to the overall behavior of cluster properties versus size, are not in satisfactory agreement with the experimental data [30]. For example, for ionization potentials, the spherical jellium yields typical saw-toothed curves, which lack fine structure between major shells, a feature that is prominent in the data. In addition, each arc of the saw-tooth rises steeply above the data before

falling sharply at the next discontinuity associated with a major-shell closure. This behavior contrasts with the observed ionization-potential (IP) curves, which remain rather flat between magic species, exhibiting a staircase profile.

The merit of the early spherical jellium model of clusters derives from the recognition of the importance of level bunching in the single-particle spectra of finite systems. The degree of level bunching is related to the degeneracies imposed by the symmetry of the systems. As is well known in various branches of physics (i.e., atomic, molecular, and nuclear physics), the high degree of degeneracy pertaining to spherical symmetry is associated with closed-shell systems. Open-shell systems, on the other hand, lower their energy via various symmetry breaking mechanisms which result in diminished degeneracies. In atomic systems, the spherical symmetry of the nuclear central-field potential felt by the electrons is broken by the repulsive inter-electron Coulomb interaction leading to a level-filling scheme favoring high-spin multiplicity according to Hund's rule [80]. In molecules (and solids), the lifting of orbital degeneracies occuring through structural distortions is known as the Jahn-Teller effect [81]. In open-shell nuclei, energy stabilization occurs via shape deformations [82, 83, 15, 3, 51] (a mechanism that may be thought of as akin to the Jahn-Teller effect).

For open-shell clusters, in analogy with atomic nuclei, it has been suggested that consideration of quadrupole shape deformations could lead to lifting of the spherical degeneracy and to an improvement in the agreement between theory and experiment. A first implementation of this idea was carried out by Clemenger [84, 85] and Saunders [86] [the Clemenger-Nilsson (CN) model], who applied to metal clusters the anisotropic, harmonic- oscillator model introduced by Nilsson [83] in nuclear physics. Unfortunately, this model does not provide a full expression for the total energy of an interacting system, and therefore cannot describe either binding energies for neutral clusters or charging energies for ionic ones. Nevertheless, in spite of such shortcomings, the CN model is still widely used to interpret the data [30, 87]. Naturally, such an interpretation is restricted to a handful of experimentally observable ground-state properties, i.e., abundances, IPs and electron affinities (EAs). Moreover, for IPs and EAs the analysis is carried out at a qualitative level by following the relative shifts of the highest-occupied-molecular-orbital (HOMO) or lowest-unoccupied-molecular-orbital (LUMO) levels.

Several Kohn-Sham-local-density-approximation (KS-LDA) studies with spheroidal jellium backgrounds [47, 88] have also been reported. Such KS calculations are rather time consuming and have been carried out only for

a small number of sodium [47, 88] and copper clusters [88] comprising less than 40 atoms and have addressed only a limited number of ground-state properties [IPs and monomer separation energies (MSEs) for Na_N, and electron affinities (EAs) for Cu_N]. Systematic theoretical results for triaxial shapes were performed only most recently [7, 89] even though there exists a wealth of experimental observations for IPs, EAs, fission dissociation energies (FDEs), as well as MSEs and dimer separation energies (DSEs), which all exhibit characteristic shell effects.

In addition to the steps at shell and subshell closures, the experimental IPs, EAs, FDEs, and MSEs exhibit a characteristic odd-even alternation, which has attracted substantial interest ([90]-[92]). One mechanism, which has been proposed [91, 92] as an explanation, involves phenomenological Cooper-pairing of electrons in analogy with the nuclear case, where nucleons form a BCS-type ground state [15, 3, 51]. However, it is difficult to justify [92] such a pairing in the case of clusters. Alternatively, for the IPs of simple metal clusters, M_N, with $N \leq 9$, such odd-even alternation has been obtained in both spheroidal jellium calculations [88] and *ab initio* quantum chemical calculations [93], suggesting that these oscillations are of a geometric (i.e., cluster-shape) origin.

The aforementioned considerations motivate investigations aiming at a systematic assessment of relationships between observed patterns and the size-evolution and dimensionality (i.e., the character and number of multipolar components) of the relevant cluster deformation spaces pertaining to the ground-state properties mentioned above. While in this study, we focus on the systematics of the influence of cluster shapes on ground-state patterns, we remark that cluster deformations have also been discussed previously in the context of optical absorption via plasmon excitations ([116],[94]-[97]).

In this subsection, we study the influence of triaxial quadrupole shapes (ellipsoids) on the ground-state properties mentioned above and provide a systematic comparison with the available experimental data (for additional comparisons, see Ref. [7]).

A SEMIEMPIRICAL SHELL-CORRECTION METHOD FOR TRIAXIALLY DEFORMED CLUSTERS

Liquid-drop model for neutral and charged deformed clusters

For neutral clusters, the liquid-drop model [98, 10, 20] (LDM) expresses the *smooth* part, $\widetilde{E}$, of the total energy as the sum of three contributions,

namely a volume, a surface, and a curvature term, i.e.,

$$\begin{aligned} \widetilde{E} &= E_{vol} + E_{surf} + E_{curv} = \\ & A_v \int d\tau + \sigma \int dS + A_c \int dS\kappa \ , \end{aligned} \tag{48}$$

where $d\tau$ is the volume element and dS is the surface differential element. The local curvature κ is defined by the expression $\kappa = 0.5(R_{max}^{-1} + R_{min}^{-1})$, where R_{max} and R_{min} are the two principal radii of curvature at a local point on the surface of the jellium droplet which models the cluster. The corresponding coefficients can be determined by fitting the extended Thomas-Fermi (ETF)-LDA total energy for spherical shapes (see section 2.1.2) to the following parametrized expression as a function of the number, N, of atoms in the cluster [99, 100],

$$E_{ETF}^{sph} = \alpha_v N + \alpha_s N^{2/3} + \alpha_c N^{1/3} \ . \tag{49}$$

The following expressions relate the coefficients A_v, σ, and A_c to the corresponding coefficients, (α's), in Eq. (49),

$$A_v = \frac{3}{4\pi r_s^3}\alpha_v \ ; \ \sigma = \frac{1}{4\pi r_s^2}\alpha_s \ ; \ A_c = \frac{1}{4\pi r_s}\alpha_c \ . \tag{50}$$

In the case of ellipsoidal shapes the areal integral and the integrated curvature can be expressed in closed analytical form with the help of the incomplete elliptic integrals $\mathcal{F}(\psi, k)$ and $\mathcal{E}(\psi, k)$ of the first and second kind [101], respectively. Before writing the formulas, we need to introduce some notations. Volume conservation must be employed, namely

$$a'b'c'/R_0^3 = abc = 1 \ , \tag{51}$$

where R_0 is the radius of a sphere with the same volume ($R_0 = r_s N^{1/3}$ is taken to be the radius of the positive jellium assuming spherical symmetry), and $a = a'/R_0$, etc..., are the dimensionless semi-axes. The eccentricities are defined through the dimensionless semi-axes as follows

$$\begin{aligned} e_1^2 &= 1 - (c/a)^2 \\ e_2^2 &= 1 - (b/a)^2 \\ e_3^2 &= 1 - (c/b)^2 \ . \end{aligned} \tag{52}$$

The semi-axes are chosen so that

$$a \geq b \geq c \ . \tag{53}$$

With the notation $\sin\psi = e_1$, $k_2 = e_2/e_1$, and $k_3 = e_3/e_1$, the relative (with respect to the spherical shape) surface and curvature energies are given [102] by

$$\frac{E_{surf}^{ell}}{E_{surf}^{sph}} = \frac{ab}{2}\left[\frac{1-e_1^2}{e_1}\mathcal{F}(\psi,k_3) + e_1\mathcal{E}(\psi,k_3) + c^3\right] \tag{54}$$

and

$$\frac{E_{curv}^{ell}}{E_{curv}^{sph}} = \frac{bc}{2a}\left[1 + \frac{a^3}{e_1}\left((1-e_1^2)\mathcal{F}(\psi,k_2) + e_1^2\mathcal{E}(\psi,k_2)\right)\right] . \tag{55}$$

The change in the smooth part of the cluster total energy due to the excess charge $\pm Z$ was already discussed by us for spherical clusters in the previous section. The result may be summarized as

$$\Delta\tilde{E}^{sph}(Z) = \tilde{E}^{sph}(Z) - \tilde{E}^{sph}(0) = \mp WZ + \frac{Z(Z \pm 0.25)e^2}{2(R_0+\delta)}, \tag{56}$$

where the upper and lower signs correspond to negatively and positively charged states, respectively, W is the work function of the metal, R_0 is the radius of the positive jellium assuming spherical symmetry, and δ is a spillout-type parameter.

To generalize the above results to an ellipsoidal shape, $\phi(R_0+\delta) = e^2/(R_0+\delta)$, which is the value of the potential on the surface of a spherical conductor, needs to be replaced by the corresponding expression for the potential on the surface of a conducting ellipsoid. The final result, normalized to the spherical shape, is given by the expression

$$\frac{\Delta\tilde{E}^{ell}(Z) \pm WZ}{\Delta\tilde{E}^{sph}(Z) \pm WZ} = \frac{bc}{e_1}\mathcal{F}(\psi,k_2) , \tag{57}$$

where the $\pm$ sign in front of WZ corresponds to negatively and positively charged clusters, respectively.

The modified Nilsson potential

A natural choice for an external potential to be used for calculating shell corrections with the Strutinsky method is an anisotropic, three-dimensional oscillator with an l^2 term for lifting the harmonic oscillator degeneracies [83]. Such an oscillator model for approximating the total energies of metal clusters, but without separating them into a smooth and a shell-correction part in the spirit of Strutinsky' s approach, has been used [30] with some

success for calculating relative energy surfaces and deformation shapes of metal clusters. However, this simple harmonic oscillator model has serious limitations, since i) the total energies are calculated by the expression $\frac{3}{4}\sum_i \varepsilon_i$, and thus do not compare with the total energies obtained from the KS-LDA approach, ii) the model cannot be extended to the case of charged (cationic or anionic) clusters. Thus absolute ionization potentials, electron affinities, and fission energetics cannot be calculated in this model. Alternatively, in our approach, we are making only a limited use of the external oscillator potential in calculating a modified Strutinsky shell correction. Total energies are evaluated by adding this shell correction to the smooth LDM energies.

In particular, a modified Nilsson Hamiltonian appropriate for metal clusters [84, 86] is given by

$$H_N = H_0 + U_0\hbar\omega_0(\mathbf{l}^2 - <\mathbf{l}^2>_n) \,, \tag{58}$$

where H_0 is the hamiltonian for a three-dimensional anisotropic oscillator, namely

$$\begin{aligned} H_0 &= -\frac{\hbar^2}{2m_e}\triangle + \frac{m_e}{2}(\omega_1^2 x^2 + \omega_2^2 y^2 + \omega_3^2 z^2) = \\ &\sum_{k=1}^{3}(a_k^\dagger a_k + \frac{1}{2})\hbar\omega_k \,. \end{aligned} \tag{59}$$

U_0 in Eq. (58) is a dimensionless parameter, which for occupied states may depend on the principal quantum number $n = n_1 + n_2 + n_3$ of the spherical-oscillator major shell associated with a given level (n_1, n_2, n_3) of the hamiltonian H_0 (for clusters comprising up to 100 valence electrons, only a weak dependence on n is found, see Table I in Ref. [7]). U_0 vanishes for values of n higher than the corresponding value of the last partially (or fully) filled major shell in the spherical limit.

$\mathbf{l}^2 = \sum_{k=1}^{3} l_k^2$ is a "stretched" angular momentum which scales to the ellipsoidal shape and is defined as follows,

$$l_3^2 \equiv (q_1 p_2 - q_2 p_1)^2 \,, \tag{60}$$

(with similarly obtained expressions for l_1 and l_2 via a cyclic permutation of indices) where the stretched position and momentum coordinates are defined via the corresponding natural coordinates, q_k^{nat} and p_k^{nat}, as follows,

$$q_k \equiv q_k^{nat}(m_e\omega_k/\hbar)^{1/2} = \frac{a_k^\dagger + a_k}{\sqrt{2}} \,, \; (k = 1, 2, 3) \,, \tag{61}$$

$$p_k \equiv p_k^{nat}(1/\hbar m_e \omega_k)^{1/2} = i\frac{a_k^\dagger - a_k}{\sqrt{2}} \ , \ (k = 1,2,3) \ . \tag{62}$$

The stretched l^2 is not a properly defined angular-momentum operator, but has the advantageous property that it does not mix deformed states which correspond to sherical major shells with different principal quantum number $n = n_1 + n_2 + n_3$ (see, the Appendix in Ref. [7] for the expression of the matrix elements of l^2).

The subtraction of the term $< l^2 >_n = n(n+3)/2$, where $< >_n$ denotes the expectation value taken over the *nth*-major shell in spherical symmetry, guaranties that the average separation between major oscillator shells is not affected as a result of the lifting of the degeneracy.

The oscillator frequencies can be related to the principal semi-axes a', b', and c' [see, Eq. (51)] via the volume-conservation constraint and the requirement that the surface of the cluster is an equipotential one, namely

$$\omega_1 a' = \omega_2 b' = \omega_3 c' = \omega_0 R_0 \ , \tag{63}$$

where the frequency ω_0 for the spherical shape (with radius R_0) was taken according to Ref. [85] to be

$$\hbar\omega_0(N) = \frac{49 \text{ eV bohr}^2}{r_s^2 N^{1/3}} \left[1 + \frac{t}{r_s N^{1/3}}\right]^{-2} \ . \tag{64}$$

Since in this paper we consider solely monovalent elements, N in Eq. (64) is the number of atoms for the family of clusters $M_N^{Z\pm}$, r_s is the Wigner-Seitz radius expressed in atomic units, and t denotes the electronic spillout for the neutral cluster according to Ref. [85].

Shell correction and averaging of single-particle spectra

Usually $\widetilde{E}_{sp}$ [see Eqs. (44) and (45)] is calculated numerically [103]. However, a variation of the numerical Strutinsky averaging method consists in using the semiclassical partition function and in expanding it in powers of $\hbar^2$. With this method, for the case of an anisotropic, fully triaxial oscillator, one finds [15, 104] an analytical result, namely [105]

$$\begin{aligned} \widetilde{E}_{sp}^{osc} &= \hbar(\omega_1\omega_2\omega_3)^{1/3} \\ &\times \left(\frac{1}{4}(3N_e)^{4/3} + \frac{1}{24}\frac{\omega_1^2+\omega_2^2+\omega_3^2}{(\omega_1\omega_2\omega_3)^{2/3}}(3N_e)^{2/3}\right) \ , \end{aligned} \tag{65}$$

where N_e denotes the number of delocalized valence electrons in the cluster.

In the present work, expression (65) (as modified below) will be substituted for the average part $\widetilde{E}_{sp}$ in Eq. (45), while the sum $\sum_i^{occ} \varepsilon_i$ will be calculated numerically by specifying the occupied single-particle states of the modified Nilsson oscillator represented by the hamiltonian (58).

In the case of an isotropic oscillator, not only the smooth contribution, $\widetilde{E}_{sp}^{osc}$, but also the Strutinsky shell correction (45) can be specified analytically, [15] with the result

$$\Delta E_{sh,0}^{Str}(x) = \frac{1}{24}\hbar\omega_0(3N_e)^{2/3}(-1 + 12x(1-x)) \,, \tag{66}$$

where x is the fractional filling of the highest partially filled harmonic oscillator shell. For a filled shell ($x = 0$), $\Delta E_{sh,0}^{Str}(0) = -\frac{1}{24}\hbar\omega_0(3N_e)^{2/3}$, instead of the essentially vanishing value as in the case of the ETF-LDA defined shell correction (cf. Fig. 1 of Ref. [7]). To adjust for this discrepancy, we add $-\Delta E_{sh,0}^{Str}(0)$ to ΔE_{sh}^{Str} calculated through Eq. (45) for the case of open-shell, as well as closed-shell clusters.

Overall procedure

We are now in a position to summarize the calculational procedure, which consists of the following steps:

1. Parametrize results of ETF-LDA calculations for spherical neutral jellia according to Eq. (49).

2. Use above parametrization (assuming that parameters per differential element of volume, surface, and integrated curvature are shape independent) in Eq. (48) to calculate the liquid-drop energy associated with neutral clusters, and then add to it the charging energy according to Eq. (57) to determine the total LDM energy $\widetilde{E}$.

3. Use Equations (58) and (59) for a given deformation [i.e., a', b', c', or equivalently ω_1, ω_2, ω_3, see Eq. (63)] to solve for the single-particle spectrum (ε_i).

4. Evaluate the average, $\widetilde{E}_{sp}$, of the single-particle spectrum according to Eq. (65) and subsequent remarks.

5. Use the results of steps 3 and 4 above to calculate the shell correction ΔE_{sh}^{Str} according to Eq. (45).

6. Finally, calculate the total energy E_{sh} as the sum of the liquid-drop contribution (step 2) and the shell correction (step 5), namely $E_{sh} = \widetilde{E} + \Delta E_{sh}^{Str}$.

The optimal ellipsoidal geometries for a given cluster $M_N^{Z\pm}$, neutral or charged, are determined by systematically varying the distortion (namely, the parameters a and b) in order to locate the global minimum of the total energy $E_{sh}(N, Z)$.

SAMPLE RESULTS

Ionization potentials

We have calculated ionization potentials by subtracting two ground-state energies, namely the ground-state energy of the neutral clusters from the ground-state energy of the singly charged cations,

$$I_{sh}(N) = E_{sh}(z = +1, N) - E_{sh}(z = 0, N) \, . \tag{67}$$

Note that the lower case z in Eq. (67) denotes the algebraic value of the excess charge, namely $z < 0$ for anions, $z > 0$ for cations, and $|z| = Z$.

Most recently, systematic measurements of the IPs of cold sodium clusters, Na_N, were performed [106]. The SE-SCM results (for N up to 105 atoms), as well as the experimental data are displayed in Fig. 12. In our introductory section, we have already shown these results for $N < 45$ [Fig. 1(c)], including SE-SCM results obtained by constraining the clusters to spherical symmetry [Fig. 1(b)] and the smooth contribution in the latter symmetry [Fig. 1(a)].

The overall agreement between theory and experiment is very satisfactory (note the close quantitative agreement of the absolute IP values). The steps at major-shell closings (N = 8, 20, 40, 58, 92), as well as those at subshell closings (N = 14, 26, 30, 34, 44, 50, 54, 68) are comparable to the experimental ones. Additionally the theoretical results reproduce well the staircase profile of the experimental curve. The overall weakening of the oscillations of the fine structure with increasing size seen in the experimental data is also portrayed by the calculations.

The odd-even oscillations are accurately reproduced for $3 \leq N \leq 21$. Above $N = 21$, however, the theory provides only a partial account for the odd-even alternations (i.e., for $N = 35 - 40$, $N = 59 - 65$, and $N = 95 - 101$). Here, experimentally observed odd-even oscillations are present

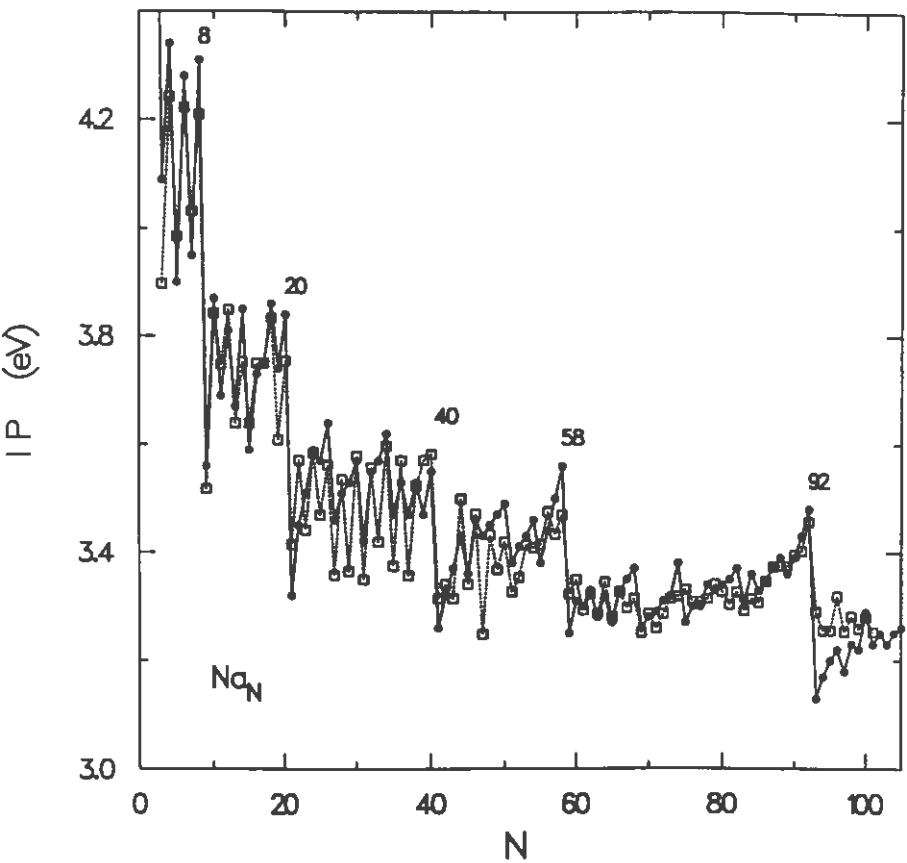

Fig. 12. IPs for Na_N clusters in the range $3 \leq N \leq 107$. Solid dots: Theoretical results derived from the SE-SCM method in conjuction with the ellipsoidal model. Open squares: Experimental measurements from Ref. [106].

throughout the $N = 21 - 40$ region and in the beginnings of the major shells immediately after $N = 40$ and $N = 58$.

Electron affinities

Electron affinities have been determined by us as the difference between two ground-state energies, namely by subtracting the ground-state energy of the singly charged anions from the ground-state energy of the neutral clusters,

$$A_{sh}(N) = E_{sh}(z = 0, N) - E_{sh}(z = -1, N) \, . \tag{68}$$

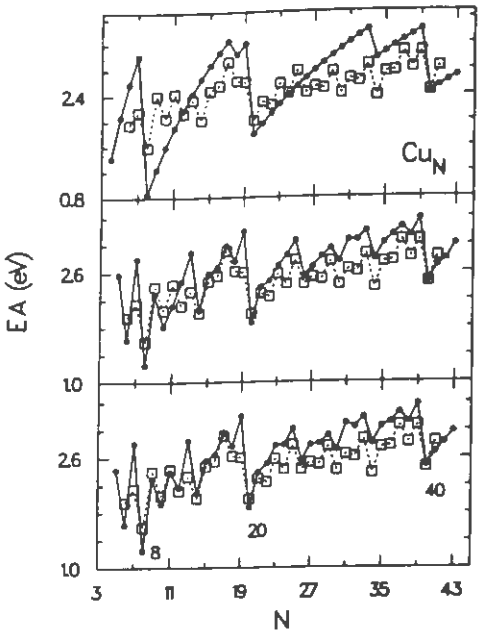

Fig. 13. EAs for Cu_N clusters in the range $5 \leq N \leq 43$. Solid dots: Theoretical results derived from the SE-SCM method. Open squares: Experimental measurements from Ref. [107]. Top panel: The spherical model compared to experimental data. Middle panel: The spheroidal model compared to experimental data. Lower panel: The ellipsoidal model compared to experimental data.

The theoretical results for Cu_N are displayed in Fig. 13, and are compared to the experimental measurements [107]. The saw-toothed profile associated with spherical jellia compares rather poorly with the experimental data. We note that the magic numbers (8, 18, 20, 34, 40) are associated with the minima of the EA curve. Noticeable improvement in the agreement between theory and experiment is achieved when spheroidal shapes are considered (middle panel). Consideration of ellipsoidal shapes (bottom panel) results in a detailed agreement between theory and experiment, mainly due to the enhancement of odd-even oscillations. In particular, the feature of strong odd-even oscillations in the range $N = 10 - 13$ together with the preservation of the quartet structure for $N = 14 - 17$ is evident, and is accounted for only by the triaxial calculations. The presence of another well-defined quartet at $N = 34 - 37$ is also accurately reproduced by the triaxial calculations. We note that triaxiality offers a detailed agreement

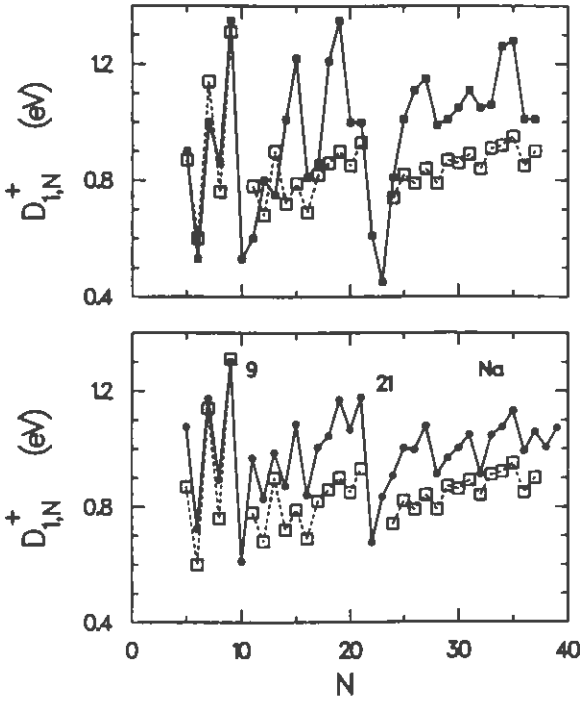

Fig. 14. Monomer separation energies, $D^+_{1,N}$ [see Eq. (69)], from singly cationic Na^+_N clusters in the range $5 \leq N \leq 39$. Open squares: Experimental measurements from Ref. [108]. Solid dots (Bottom panel): Theoretical results derived from the SE-SCM method. Solid squares (Top panel): Theoretical results according to the KS-LDA spheroidal calculations of Ref. [47].

for the odd-even alternations in the EA curve of Cu_N up to $N = 41$.

Monomer separation energies

Monomer separation energies associated with the unimolecular reaction $Na^+_N \rightarrow Na^+_{N-1}$+Na have been calculated as follows

$$D^+_{1,N} = E_{sh}(z = +1, N-1) + E_{sh}(z = 0, N = 1) - E_{sh}(z = +1, N)\,. \quad (69)$$

The theoretical and experimental [108] results for $D^+_{1,N}$ for sodium are displayed at the bottom panel of Fig. 14. From our calculations, we find, as for the case of IPs and EAs, that results obtained via calculations restricted

to spherical shapes compare rather poorly with the experiment, that improvement is achieved when spheroidal deformations are considered, and that the agreement between theory and experiment becomes detailed when triaxiality is taken into consideration. The feature of the appearance of strong odd-even alternations for $N = 12 - 15$ (note the one-unit shift due to the single positive excess charge) together with a well-defined quartet in the range $N = 16 - 19$ is present in the monomer separation energies.

We also include for comparison results obtained by KS-LDA calculations [47] for deformed Na_N clusters restricted to axial (spheroidal) symmetry (Fig. 14, top panel). As expected, except for very small clusters ($N < 9$), these results do not exhibit odd-even oscillations. In addition, significant discrepancies between the calculated and experimental results are evident, particularly pertaining to the amplitude of oscillations at shell and subshell closures.

Fission energetics

Fission of doubly charged metal clusters, $M_N^{2\pm}$, has attracted considerable attention in the last few years. Nevertheless, LDA calculations have been restricted to spherical jellia for both parent and daughters, [109, 110] with the exception of molecular-dynamical calculations for sodium [43] and potassium [111] clusters with $N \leq 12$. We present here systematic calculations for the dissociation energies $\Delta_{N,P}$ of the fission processes $K_N^{2+} \rightarrow K_P^+ + K_{N-P}^+$, as a function of the fission channels P.

We have calculated the dissociation energies

$$\begin{aligned} \Delta_{N,P} &= E_{sh}(z = +1, P) + E_{sh}(z = +1, N - P) \\ &\quad - E_{sh}(z = +2, N) \, , \end{aligned} \tag{70}$$

for the case of a parent cluster having $N = 26$ potassium atoms, for which corresponding experimental results [112] are available. The theoretical calculations compared to the experimental results are displayed in Fig. 15. Again, while consideration of spheroidal shapes improves greatly the agreement between theory and experiment over the spherical model, fully detailed correspondence is achieved only upon allowing for triaxial-shape deformations (notice the improvement in the range $P = 12 - 14$). We note that the magic fragments K_3^+ and K_9^+ correspond to strong minima.

Cluster shapes

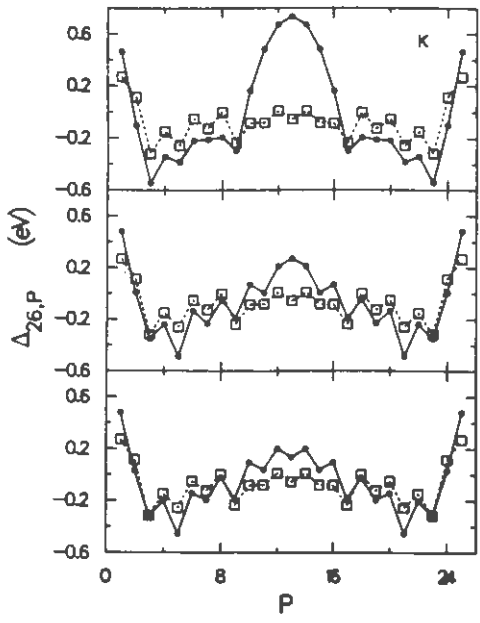

Fig. 15. Fission dissociation energies, $\Delta_{26,P}$ [see Eq. (70)], for the doubly cationic K_{26}^{2+} cluster as a function of the fission channels P. Solid dots: Theoretical results derived from the SE-SCM method. Open squares: Experimental measurements from Ref. [112]. Top panel: The spherical model compared to experimental data. Middle panel: The spheroidal model compared to experimental data. Lower panel: The ellipsoidal model compared to experimental data.

In this subsection, we present systematics of the Na_N equilibrium triaxial shapes in the range $3 \leq N \leq 60$. A most economical way for such a presentation is through the use of the Hill-Wheeler parameters [113] β and γ, which are related to the dimensionless semi-axes a, b, and c [see, Eq. (51)] as follows,

$$\begin{aligned} a &= \exp\left[\sqrt{5/(4\pi)}\,\beta\cos\left(\gamma - \frac{2\pi}{3}\right)\right] \\ b &= \exp\left[\sqrt{5/(4\pi)}\,\beta\cos\left(\gamma + \frac{2\pi}{3}\right)\right] \\ c &= \exp\left[\sqrt{5/(4\pi)}\,\beta\cos\gamma\right], \end{aligned} \tag{71}$$

where β is unrestricted and $0 \leq \gamma \leq \pi/3$. A value $\gamma \neq 0$ indicates a triaxial shape, while $\gamma = 0$ corresponds to a prolate shape, and $\gamma = \pi/3$ denotes

an oblate deformation. The origin corresponds to spherical shapes.

Using the above definitions, the cluster potential energy surfaces (PESs) in deformation space may be easily mapped and studied. In this manner, one can analyze the topography of the PESs, identify global as well as local minima (i.e., shape isomers), barriers separating them, and paths in deformation space by which they may transform to each other. Since the values of ground-state properties of clusters depend on the shape of the cluster, the existence of shape isomers may be manifested in experimental measurements. For example, in the case of measurements of ionization potentials, vertical ionization of a cluster M_N (e.g., starting from its optimal ground-state configuration, or close to it) results in a M_N^+ cluster in the configuration of the parent neutral. If the M_N^+ cluster possesses shape isomers, it may relax either to the optimal configuration (global minimum) or to a local minimum (shape isomer), depending on the relationship between the topology of the PES for the M_N^+ cluster and that of the M_N parent. These two channels will lead to different values for the adiabatic IP. Moreover, the measured IP value may depend on the internal energy of the cluster (i.e., internal kinetic energy, or temperature), since the rate of shape transformations is expected to be enhanced at higher temperatures (i.e., at low temperature the cluster may be trapped at local minima in "shape-space"). We suggest that measurements of cluster properties, and their temperature dependence, may provide information about the topology of the PESs of clusters in shape-space. Indeed, evidence for the occurence of structural isomers has been inferred from photoionization studies [114] of Niobium clusters, where multiple ionization energies were measured for Nb_9 and Nb_{12}, and from kinetic studies [114, 115] of the reactivity behavior of Niobium clusters reacting with D_2.

The PESs for Na_{12}, Na_{13}, and Na_{14} are shown in Fig. 16 using the Hill-Wheeler parametrization. First we note that all three clusters possess at least one shape isomer. For Na_{12}, the optimal shape is triaxially deformed and is separated by a potential barrier of approximately 0.5 eV from a shallow oblate isomer. On the other hand for Na_{13}, while the optimal shape is triaxial close to the prolate axis, there exists a triaxial shape isomer close to the oblate axis. We note that the energy difference between the two minima is very small, reflecting the fact that the topology of the PES of Na_{13} is characterized by a very flat valley in the γ coordinate. This is correlated with the insensitivity of the total energy of this cluster calculated via the spheroidal and ellipsoidal models. In this context, we remark that the above observation concerning the flat nature of the Na_{13} PES is in agreement with conclusions drawn from LDA molecular-dynamics

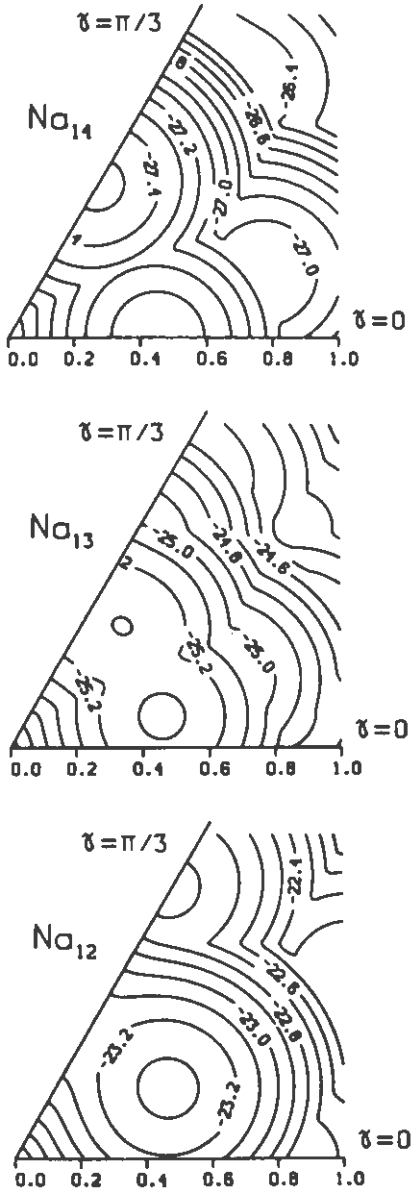

Fig. 16. PESs (according to the ellipsoidal model) for the neutral Na_{12} (bottom panel), Na_{13} (middle panel), and Na_{14} (top panel) clusters. The radius (β) and the angle γ are the Hill-Wheeler quadrupole deformation parameters. The scale of β is marked on the horizontal axes. The contour lines correspond to increments of 0.1 eV in the total energy of the clusters.

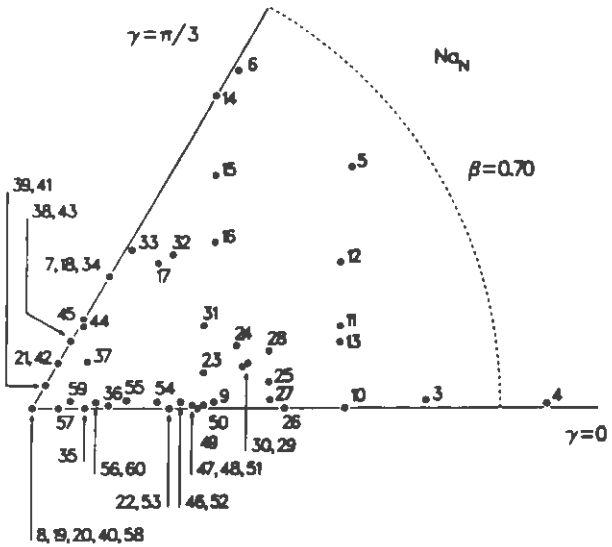

Fig. 17. The Hill-Wheeler parameters specifying the equilibrium shapes (corresponding to the global minima of the PESs) of neutral Na_N clusters according to the ellipsoidal model in the range $3 \leq N \leq 60$.

calculations [44]. Finally, the PES for Na_{14} exhibits two axially symmetric minima, with the global one being the oblate shape.

In Fig. 17, we present the Hill-Wheeler parameters which correspond to the global minima of the total energy of the clusters within our SE-SCM approach. We note that, as a result of allowing for ellipsoidal deformations, many clusters assume well developed triaxial shapes, most notably Na_5, Na_{11}, Na_{12}, Na_{13}, Na_{16}, etc. Overall the extent of deformation decreases with increasing size, as reflected in the diminishing values of the β parameter. As expected, clusters associated with major-shell closures lie at the origin (i.e., they are spherical), except Na_{18} which has an oblate shape.

Unlike the present work, where deformed shapes are inferred through ground-state properties, earlier this was usually done through photoabsorption measurements [30, 116, 95]. Indeed, phenomenological models assign a different absorption energy for each axis and divide the oscillator strength equally among them (1/3 each in the case of the three axes of an ellipsoid and 2/3 and 1/3 in the case of a spheroid). These phenomenological models relate directly the resulting splitting of the plasmon line to the semi-axes [and through equations (71) to the Hill-Wheeler parameters β and γ] and do not require prior knowledge, or make explicit use, of the quantal struc-

ture of the clusters, as is the case with calculations based on evaluation of the total energies.

Recently, a systematic inference of shapes of Na_N^+ clusters has been carried out [95] through an attempt to draw a direct connection between shape deformations, which were presumed spheroidal, and measured photoabsorption cross sections (which were accordingly fitted with at most two Lorentz functions). Focusing on the cluster range $N = 11 - 21$ – where our results for ground-state properties for all metal clusters studied here (especially, sodium clusters) provide a detailed description of available experimental data – we find discrepancies between the shapes predicted from our approach and those suggested in Ref. [95]. For example, while in Ref. [95] prolate shapes were assigned to Na_{14}^+ and Na_{15}^+, and a spherical shape to Na_{16}^+, our results yield a triaxial, an oblate, and again a triaxial shape, respectively (note the shift by one unit in N with respect to the neutral clusters of Fig. 17). This suggests that utmost caution must be applied when shapes are inferred from experimental fits of optical absorption cross sections in conjunction with certain phenomenological models. Indeed, the difficulty in interpreting the optical cross sections is due to a strong broadening [117] of each absorption line, which can mask the plasmon splitting due to the deformation. In this context, we remark that our SE-SCM yielded results in overall agreement with the triaxial shapes inferred from the simple Clemenger-Nilsson model [86, 30], which has been used previously in the analysis of photoabsorption cross sections [116], for clusters with $N \leq 40$.

3.2.2 Electronic shell effects in fission barriers and fission dynamics of metal clusters

Fragmentation and fission processes underly physical and chemical phenomena in a variety of systems, characterized by a wide spectrum of energy scales, nature of interactions, and characteristic spatial and temporal scales. These include nuclear fission [15, 3], fragmentation, unimolecular decay and reactions in atomic and molecular systems [118], and more recently fission of atomic and molecular clusters ([10, 43, 98, 110, 111],[119]-[121]) Investigations of energetics, mechanisms, pathways, and dynamics of fission processes provide ways and means for explorations of structure, stability, excitations, and dynamics in multi-body (finite) systems, as well as allow for comprehensive tests of theoretical methodologies and conceptual developments, and have formed active areas of fruitful research endeavors in nuclear physics, and more recently in cluster science. Therefore, we focus

our discussion on recent trends in studies of fission processes in metal clusters, and comment on issues pertaining to analogies and differences between such processes and those encountered in nuclear systems.

Multiply charged metallic clusters (M_n^{x+}) are observable in mass spectra if they exceed a critical size of stability n_c^{x+} (e.g. for $x = 2$, $n_c^{2+} = 27$ for Na and $n_c^{2+} = 19$ for K [119]). For clusters with $n > n_c^{x+}$, evaporation of neutral species is the preferred dissociation channel, while, below the critical size, fission into two charged fragments dominates (for $x = 2$, two singly charged fragments emerge). Nevertheless, at low enough temperature, such M_n^{x+} ($n < n_c^{x+}$) clusters can be metastable above a certain size n_b^{x+}, because of the existence of a fission barrier E_b (for Na_n^{2+} and K_n^{2+}, $n_b^{2+} = 7$ [43, 111]).

These observations indicate that fission of metal clusters occurs when the repulsive Coulomb forces due to the accumulation of the excess charges overcome the electronic binding (cohesion) of the cluster. This reminds us immediately of the well-studied nuclear fission phenomenon and the celebrated Liquid Drop Model (LDM) according to which the binding nuclear forces are expressed as a sum of volume and surface terms, and the balance between the Coulomb repulsion and the increase in surface area upon volume conserving deformations allows for an estimate of the stability and fissility of the nucleus [122, 123].

Before discussing the LDM (and variants thereof), and its adaptability to the description of cluster fission, we note that for atomic and molecular clusters microscopic descriptions of energetics and dynamics of fission processes, based on modern electronic structure calculations in conjunction with molecular dynamics (MD) simulations (where the classical trajectories of the ions, moving on the concurrently calculated Born-Oppenheimer (BO) electronic potential energy surface, are obtained via integration of the Newtonian equations of motion), are possible and have been performed [43, 111] [for a detailed description of the BO-LSD-MD method, see Barnett, R.N. and Landman, U. (1993) *Phys. Rev. B* **48**, 2081]. Such calculations, using norm-conserving non-local pseudopotentials and self-consistent solutions of the Kohn-Sham local spin-density functional (LSD) equations [43, 111], applied to small sodium [43] and potassium [111] clusters, revealed several important trends (Figs. 18 – 20): (i) The energetically favorable fission channel for such doubly-charged clusters is the asymmetric one, $M_n^{2+} \rightarrow M_{n-3}^{+} + M_3^{+}$, containing a "magic" daugther M_3^{+} (M = Na, K), i.e., $\Delta_m = E(M_{n-m}^{+}) + E(M_m^{+}) - E(M_n^{2+})$ is smallest for $m = 3$; (ii) Fission of clusters with $n \geq n_b^{2+}$, where $n_b^{2+} = 7$, involves barriers, whose magnitudes reflect the closed-shell stability of the parent cluster (i.e., E_b for $n = 10$ is particularly high), exhibiting a double-hump barrier shape [see,

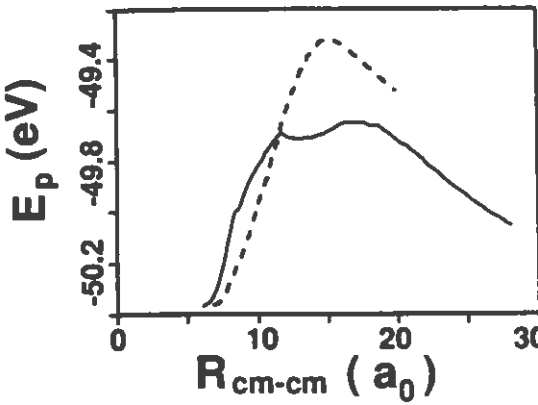

Fig. 18. Molecular dynamics results for the potential energy vs distance (in atomic units) between the centers of mass for the fragmentation of Na_{10}^{2+} into Na_7^+ and Na_3^+ (solid) and Na_9^+ and Na^+ (dashed), obtained via constrained minimization of the LSD ground-state energy of the system [43].

Figs. 18 and 20(a)]; (iii) The eventual fission products may be distinguishable (i.e., preformed) already at a rather early stage of the fission process (on the top of the exit barrier for Na_{10}^{2+}, see Fig. 19, or prior to the exit barrier for K_{12}^{2+}, see Fig. 20), and the electronic binding between the two fragments is long-range in nature; (iv) The kinetic energy release $\mathcal{E}_r$ in the favorable channel obtained via dynamic simulations was found to be given by $\mathcal{E}_r \approx E_b + |\Delta_3|$, and the results are in correspondence with experimental measurements [111] for K_n^{2+} $(5 \leq n \leq 12)$. Furthermore, in agreement with experimental findings, the emerging fragments are vibrationally excited, with the heating of the internal nuclear degrees of freedom of the fission products in the exit channel originating from dynamical conversion of potential into internal kinetic energy [see, K_{9+}^{int} in Fig. 20(b)].

Several of the trends exhibited by the microscopic calculations (such as influence of magic numbers, associated with electronic shell closing, on fission energetics and barrier heights; predominance of an asymmetric fission channel; double-hump fission-barrier shapes; shapes of deforming clusters along the fission trajectory portraying two fragments connected through a stretching neck) suggest that appropriate adaptation of methodologies developed originally in the context of nuclear fission may provide a useful conceptual and calculational framework for studies of systematics and patterns of fission processes in metallic clusters.

We comment first on the earliest treatments of pertinent nuclear processes, i.e., fission [122, 15] and alpha radioactivity [124, 125, 3]. Adap-

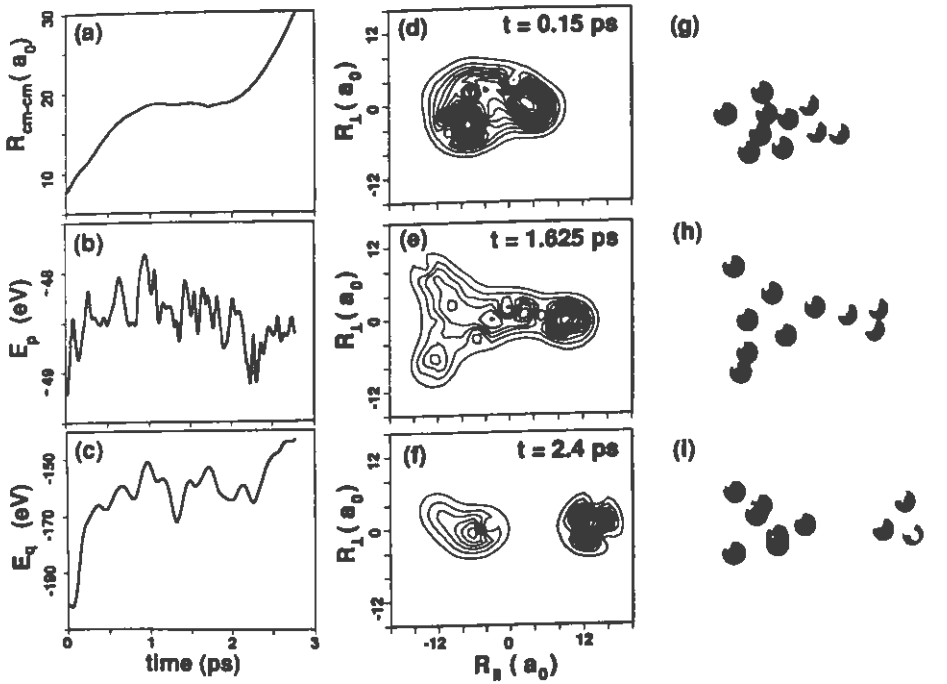

Fig. 19. Fragmentation dynamics of Na_{10}^{2+} from first-principles Born-Oppenheimer Local-spin-density functional Molecular-dynamics simulations [43]. (a)-(c) Center-of-mass distance between the eventual fission products ($R_{c.m.-c.m.}$), total potential energy (E_p), and the electronic contribution E_q to E_p, vs time. (d)-(f) Contours of the total electronic charge distribution at selected times calculated in the plane containing the two centers of mass. The $R_{||}$ axis is parallel to $\mathbf{R}_{c.m.-c.m.}$. (g)-(i) Cluster configurations for the times given in (d)-(f). Dark and light balls represent ions in the large and small fragments, respectively. Energy, distance, and time in units of eV, bohr (a_0), and ps, respectively.

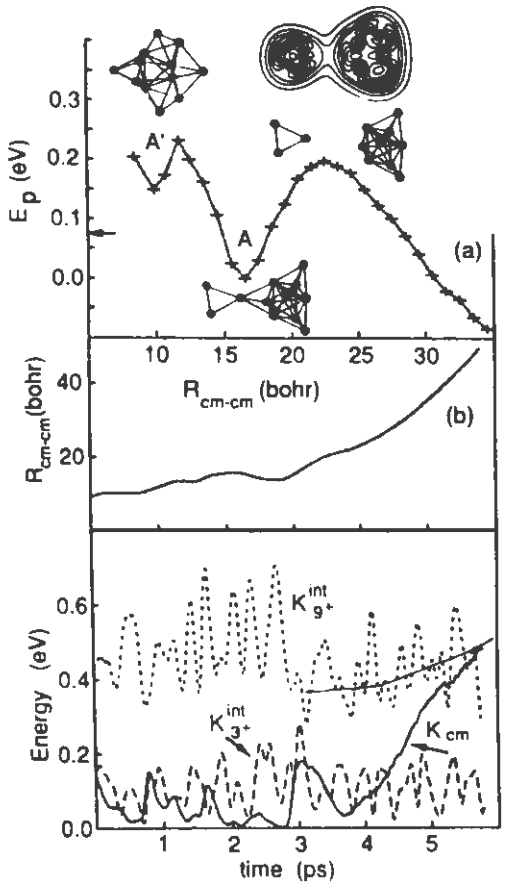

Fig. 20. (a) Potential energy of K_{12}^{2+} fissioning in the favorable channel ($K_3^+ + K_9^+$) versus the inter-fragment distance $R_{c.m.-c.m.}$ obtained via constrained minimization. The origin of the E_p scale is set at the optimal pre-barrier configuration (A). For large $R_{c.m.-c.m.}$, E_p=−0.9 eV, i.e., Δ_3. Included also are cluster configurations of K_{12}^{2+} corresponding to: a compact isomer (A′) (the energy of the optimal compact isomer found is denoted by an arrow); the optimal bound configuration (A); the structure on top of the exit-channel barrier for which contours of the total electronic charge density, ρ, are shown[111].

(b) Time evolution of $R_{c.m.-c.m.}$, the internal vibrational kinetic energies of the fragments (K_{3+}^{int} and K_{9+}^{int}) and the sum of the fragments translational kinetic energies (K_{cm}) obtained via a BO-LSD-MD simulation starting from ionization ($t = 0$) of a K_{12}^+ cluster at 500 °K. A line is drawn in K_{9+}^{int} (for $t \geq 3$ ps) to guide the eye, illustrating heating of the internal vibrational degrees of freedom of the departing fragment.

tation of the simple one-center LDM to charged metallic clusters [98], involving calculation of the Coulomb repulsive energy due to an excess charge localized at the surface, yields a reduced LDM fissility parameter $\xi = (x^2/n)/(x^2/n)_{cr}$, where $(x^2/n)_{cr} = 16\pi r_s^3\sigma/e^2$ with the surface energy per unit area denoted by σ (using bulk r_s and σ values, $(x^2/n)_{cr} = 0.44$ and 0.39 for K_n^{x+} and Na_n^{x+}, respectively). Accordingly, a cluster is unstable for $\xi > 1$ (implying that for K_n^{2+} with $n \leq 9$ and Na_n^{2+} with $n \leq 10$ barrierless fission should occur) with the most favorable channel being the symmetric one (i.e., when the two fragments have equal masses, which is only approximately true for nuclear fission, and certainly not the case for small metal clusters). For $0.351 < \xi < 1$, the system is metastable (i.e., may fission in a process involving a barrier), and for $0 < \xi < 0.351$ the system is stable.

At the other limit, α-radioactivity, which may be viewed as an extreme case of (superasymmetric) fission, is commonly described as a process where the fragments are formed (or as often said, preformed) before the system reaches the top of the barrier (saddle point), and as a result the barrier is mainly Coulombic [3]. We note here that asymmetric emission of heavier nuclei is also known (e.g., $^{223}Ra \rightarrow {}^{14}C + {}^{209}Pb$, referred to as exotic or cluster radioactivity [126, 127, 128]), and the barriers in these cases resemble the one-hump barrier of alpha radioactivity and do not exhibit modulations due to shell effects [128]. We also remark that such α-radioactivity-type (essentially Coulombic) barriers have been proposed recently [110] for describing the overall shape of the fission barriers in the case of metal clusters.

Although several aspects of the simple LDM (e.g., competition between Coulomb and surface terms) and the α-particle, Coulombic model (e.g., asymmetric channels and a scission configuration close to the location of the saddle of the multi-dimensional potential-energy surface) are present in the fission of metal clusters, neither model is adequate in light of the characteristic behavior revealed from the microscopic calculations and experiments discussed earlier. Rather, we find that proper treatments of fission in these systems require consideration of shell effects (for a recent experimental study that demonstrates the importance of shell effects in metal-cluster fission, see Ref. [119b]). While such effects are known to have important consequences in nuclear fission (transforming the one-hump LDM barrier for symmetric fission into a two-hump barrier [129, 3]), their role in the case of metal clusters goes even further. Indeed, as illustrated below for the case of the magic Na_{10}^{2+}, shell effects can be the largest contribution to the fission barrier, even in instances when the LDM component exhibits no barrier (in this case the LDM fissility $\xi > 1$). In this respect, Na_{10}^{2+} is analogous to

the case of superheavy nuclei, which are believed [130] to be stabilized by the shell structure of a major shell closure at $Z = 114$, $N = 184$ (Z is the number of protons and N is the number of neutrons; unfortunately such nuclei have not been yet observed or synthesized artificially).

The method we adopt for studying metal-cluster fission is a generalization of the semi-empirical shell correction method (SE-SCM) described in section 3.2.1 (see also Ref. [7]).

As discussed above (see section 3.2.1), in the SE-SCM method we need to introduce appropriate model potentials. As will become apparent from our results, one-center potentials (like the one-center anisotropic harmonic oscillator of Ref. [7]) are not adequate for describing shell effects in the fission of small metal clusters; rather, a two-center potential is required. Indeed, the model potentials should be able to simulate the fragmentation of the initial parent cluster towards a variety of asymptotic daugther-cluster shapes, e.g., two spheres in the case of double magic fragments, a sphere and a spheroid in the case of a single magic fragment, or two spheroids in a more general case. In the case of metal clusters, asymmetric channels are most common, and thus a meaningful and flexible description of the asymmetry is of primary concern. We found [8, 9] that such a required degree of flexibility can be provided via the shape parametrization of the asymmetric two-center-oscillator shell model (ATCOSM) introduced earlier in nuclear fission [131].

In addition to the present shape parametrization [8, 9], other two-center shape parametrizations [mainly in connection with Kohn-Sham local density functional (KS-LDA) jellium calculations] have been used ([132]-[134]) in studies of metal cluster fission. They can be grouped into two categories, namely, the two-intersected-spheres jellium [132, 135], and the variable-necking-in parametrizations [133, 134]. In the latter group, Ref. [133] accounts for various necking-in situations by using the "funny-hills" parametrization [136], while Ref. [134] describes the necking-in by connecting two spheres smoothly through a quadratic surface. The limitation of these other parame- trizations is that they are not flexible enough to account for the majority of the effects generated by the shell structure of the parent and daughters, which in general do not have spherical, but deformed (independently from each other), shapes. An example is offered by the case of the parent Na_{18}^{2+}, which has a metastable oblate ground state, and thus cannot be described by any one of the above parametrizations. We wish to emphasize again that one of the conclusions of the present work is that the shell structures of the (independently deformed) parent and daughters are the dominant factors specifying the fission barriers, and thus parametriza-

tions ([132]-[134]) with restricted final fragments (or parent) shapes are deficient in accounting for some of the most important features governing metal-cluster fission.

ASYMMETRIC TWO-CENTER OSCILLATOR MODEL

In the ATCOSM approach, the single-particle levels, associated with both the initial one-fragment parent and the separated daughters emerging from cluster fission, are determined by the following single-particle hamiltonian [131, 137],

$$H = T + \frac{1}{2}m_e\omega_{\rho i}^2\rho^2 + \frac{1}{2}m_e\omega_{zi}^2(z - z_i)^2 + V_{neck}(z) + U(\mathbf{l}_i^2) \,, \qquad (72)$$

where $i = 1$ for $z < 0$ (left) and $i = 2$ for $z > 0$ (right).

This hamiltonian is axially symmetric along the z axis. ρ denotes the cylindrical coordinate perpendicular to the symmetry axis. The shapes described by this Hamiltonian are those of two semispheroids (either prolate or oblate) connected by a smooth neck [which is specified by the term $V_{neck}(z)$]. $z_1 < 0$ and $z_2 > 0$ are the centers of these semispheroids. For the smooth neck, the following $4th$-order expression [137] was adopted, namely

$$V_{neck}(z) = \frac{1}{2}m_e\xi_i\omega_{zi}^2(z - z_i)^4\theta(|z| - |z_i|) \,, \qquad (73)$$

where $\theta(x) = 0$ for $x > 0$ and $\theta(x) = 1$ for $x < 0$.

The frequency $\omega_{\rho i}$ in Eq. (72) must be z-dependent in order to interpolate smoothly between the values $\omega_{\rho i}^{\circ}$ of the lateral frequencies associated with the left ($i = 1$) and *right* ($i = 2$) semispheroids, which are not equal in asymmetric cases. The frequencies $\omega_{\rho i}^{\circ}$ ($i = 1, 2$) characterize the lateral harmonic potentials associated with the two semispheroids outside the neck region. In the implementation of such an interpolation, we folllow Ref. [137].

The angular-momentum dependent term $U(\mathbf{l}_i^2)$, where $\mathbf{l}_1$ and $\mathbf{l}_2$ are pseudoangular momenta with respect to the left and *right* centers z_1 and z_2, is a direct generalization of the corresponding term familiar from the one-center Nilsson potential (e.g., see Ref. [7]. Its function is to lift the usual harmonic-oscillator degeneracies for different angular momenta, that is, for a spherical shape the $1d - 2s$ degeneracy is properly lifted into a $1d$ shell that is lower than the $2s$ shell (for the parameters entering into this term, which ensure a proper transition from the case of the fissioning cluster to that of the separated two fragments, we have followed Ref. [137]).

The cluster shapes associated with the spatial-coordinate-dependent single-particle potential $V(\rho, z)$ in the hamiltonian (72) are determined by the assumption that the cluster surface coincides with an equipotential surface of value V_0, namely, from the relation $V(\rho, z) = V_0$. Subsequently, one solves for ρ and derives the cluster shape $\rho = \rho(z)$. For the proper value of V_0, we take the one associated with a spherical shape containing the same number of atoms, N_Z, as the parent cluster, namely, $V_0 = \frac{1}{2} m_e \omega_0^2 R^2$, where $\hbar\omega_0 = 49 r_s^{-2} N_Z^{-1/3}$ eV, $R = r_s N_Z^{1/3}$, and r_s is the Wigner-Seitz radius. Volume conservation is implemented by requiring that the volume enclosed by the fissioning cluster surface (even after separation) remains equal to $4\pi R^3/3$.

The cluster shape in this parametrization is specified by four independent parameters. We take them to be: the separation $d = z_2 - z_1$ of the semispheroids; the asymmetry ratio $q_{as} = \omega_{\rho 2}^{\circ}/\omega_{\rho 1}^{\circ}$; and the deformation ratios for the left (1) and right (2) semispheroids $q_i = \omega_{zi}/\omega_{\rho i}^{\circ}$ $(i = 1, 2)$.

The single-particle levels of the hamiltonian in Eq. (72) are obtained by numerical diagonalization in a basis consisting of the eigenstates of the following auxiliary hamiltonian:

$$H_0 = T + \frac{1}{2} m_e \overline{\omega}_\rho^2 \rho^2 + \frac{1}{2} m_e \omega_{zi}^2 (z - z_i)^2 \ , \tag{74}$$

where $\overline{\omega}_\rho$ is the arithmetic average of $\omega_{\rho 1}^{\circ}$ and $\omega_{\rho 2}^{\circ}$. The eigenvalue problem specified by the auxiliary hamiltonian (74) is separable in the cylindrical variables ρ and z. The general solutions in ρ are those of a two-dimensional oscillator, while in z they can be expressed through the parabolic cylinder functions [138]. The matching conditions at $z = 0$ for the left and right domains yield the z-eigenvalues and the associated eigenfunctions [131].

Having obtained the single-particle spectra, the empirical shell correction (in the spirit of Strutinsky's method [2]), ΔE_{sh}^{Str}, is determined from Eq. (45).

The single-particle average, E_{av}^{Str} [i.e., $\widetilde{E}_{sp}$ in Eq. (45)], is calculated [139] through an $\hbar$ expansion of the semiclassical partition function introduced by Wigner and Kirkwood. For general-shape potentials, this last method amounts [139] to eliminating the semiclassical Fermi energy $\widetilde{\lambda}$ from the set of the following two equations

$$N_e = \frac{1}{3\pi^2} \left(\frac{2m_e}{\hbar^2} \right)^{3/2} \int^{\mathbf{r}_{\widetilde{\lambda}}} d\mathbf{r} \left[(\widetilde{\lambda} - V)^{3/2} - \frac{1}{16} \frac{\hbar^2}{2m_e} (\widetilde{\lambda} - V)^{-1/2} \nabla^2 V \right] \ , \tag{75}$$

and

$$E_{av}^{Str} = \frac{1}{3\pi^2}\left(\frac{2m_e}{\hbar^2}\right)^{3/2}\int^{\mathbf{r}_{\tilde{\lambda}}} d\mathbf{r}\left(\left[\frac{3}{5}(\tilde{\lambda}-V)^{5/2}+V(\tilde{\lambda}-V)^{3/2}\right]\right.$$
$$\left.+\frac{1}{16}\frac{\hbar^2}{2m_e}\left[(\tilde{\lambda}-V)^{1/2}\nabla^2 V - V(\tilde{\lambda}-V)^{-1/2}\nabla^2 V\right]\right) , \quad (76)$$

where N_e is the total number of delocalized valence electrons, and $V(\rho, z)$ is the potential in the single-particle hamiltonian of Eq. (72). The domain of integration is demarcated by the classical turning point $\mathbf{r}_{\tilde{\lambda}}$, such that $V(\mathbf{r}_{\tilde{\lambda}}) = \tilde{\lambda}$.

Finally, from the liquid-drop-model (LDM) contributions, we retain the two most important ones, namely the surface contribution and the Coulomb repulsion. To determine the surface contribution, we calculate numerically the area of the surface of the fissioning cluster shape, $\rho = \rho(z)$, and multiply it by a surface-tension coefficient specified via an Extended-Thomas-Fermi (ETF) -LDA calculation for spherical jellia [4, 5, 7, 8]. The Coulomb repulsion is calculated numerically using the assumption of a classical conductor (for a more elaborate application of the LDM to triaxially deformed ground states of neutral and charged metal clusters described via a one-center shape parametrization, see our discussion in section 3.2.1 in connection with Eqs. (48-57) and Ref. [7]).

In brief, the total energy E_{total} is given by

$$E_{total} = E_{LDM} + \Delta E_{sh}^{Str} = E_S + E_C + \Delta E_{sh}^{Str} , \quad (77)$$

where E_S and E_C are the surface and Coulomb terms, respectively.

RESULTS

As a demonstration of our method, we present results for two different parents, namely Na_{10}^{2+}, Na_{18}^{2+}.

Fig. 21 presents results for the channel $Na_{10}^{2+} \rightarrow Na_7^+ + Na_3^+$ for three different cases, namely, when the larger fragment, Na_7^+, is oblate (left column), spherical (middle column), and prolate (right column). From our one-center analysis, we find as expected that Na_7^+ (six electrons) has an oblate global minimum and a higher in energy prolate local minimum. In the two-center analysis, we have calculated the fission pathways so that the emerging fragments correspond to possible deformed one-center minima. It is apparent that the most favored channel (i.e., having the lowest barrier,

see the solid line in the bottom panels) will yield an oblate Na_7^+ (left column in Fig. 21), in agreement with the expectations from the one-center energetics analysis.

The middle panels exhibit the decomposition of the total barrier into the three components of surface, Coulomb, and shell-correction terms [see Eq. (77)], which are denoted by an upper dashed curve, a lower dashed curve, and a solid line, respectively. The total LDM contribution (surface plus Coulomb) is also exhibited at the bottom panels (dashed lines).

It can be seen that the LDM barrier is either absent or very small, and that the total barrier is due almost exclusively to electronic shell effects. The total barrier has a double-humped structure, with the outer hump corresponding to the LDM saddle point, which also happens to be the scission point (indicated by an empty vertical arrow). The inner hump coincides with the peak of the shell-effect term, and is associated with the rearrangement of single-particle levels from the initial spherical parent to a molecular configuration resembling a Na_7^+ attached to a Na_3^+. Such molecular configurations (discovered earlier in *ab initio* molecular-dynamics simulations [43, 111, 8] of fission of charged metal clusters, as well as in studies of fusion of neutral clusters [140]) are a natural precursor towards full fragment separation and complete fission, and naturally they give rise to the notion of preformation of the emerging fragments [43, 111, 8].

Fig. 22(a) displays the ATCOSM results for the symmetric channel $Na_{18}^{2+} \rightarrow 2Na_9^+$ (this channel is favored compared to that of the trimer, both from energetics and barrier considerations), when, for illustrative purposes, the parent is assumed to be spherical at $d = 0$. The top panel of Fig. 22(a) describes the evolution of the single-particle spectra. The spherical ordering $1s$, $1p$, $1d$, $2s$, etc., for the parent at $d = 0$ is clearly discernible. With increasing separation distance, the levels exhibit several crossings, and, after the scission point, they naturally regroup to a new ordering associated with the spherical Na_9^+ products (at the end of the fission process, the levels are doubly degenerate compared to the initial configuration, since there are two Na_9^+ fragments). It is seen that the ATCOSM leads to an oscillator energy (i.e., the gap between two populated major shells exhibited at the right end of the figure) of 1.47 eV for each Na_9^+ fragment in agreement with the value expected from the one-center model [the $1s$ state of Na_9^+ lies at 2.21 eV; in the case of the initial spherical Na_{18}^{2+} ($d = 0$), the oscillator energy corresponding to the gap between major shells is 1.17 eV, and the corresponding $1s$ state lies at 1.75 eV].

From the middle panel of Fig. 22(a), we observe that the shell-correction (solid line) contributes a net gain in energy of about 1.6 eV upon dissocia-

Fig. 21. ATCOSM results for the asymmetric channel $Na_{10}^{2+} \rightarrow Na_7^+ + Na_3^+$. The final configuration of Na_3^+ is spherical. For the heavier fragment Na_7^+, we present results associated with three different final shape configurations, namely, oblate [(o,s); left], spherical [(s,s); middle], and prolate [(p,s); right]. The ratio of shorter over longer axis is 0.555 for the oblate case and 0.75 for the prolate case.

Bottom panel: LDM energy (surface plus Coulomb, dashed curve) and total potential energy (LDM plus shell corrections, solid curve) as a function of fragment separation d. The empty vertical arrow marks the scission point. The zero of energy is taken at $d = 0$. A number (-1.58 eV or -0.98 eV), or a horizontal solid arrow, denotes the corresponding dissociation energy.

Middle panel: Shell-correction contribution (solid curve), surface contribution (upper dashed curve), and Coulomb contribution (lower dashed curve) to the total energy, as a function of fragment separation d.

Top panel: Single-particle spectra as a function of fragment separation d. The occupied (fully or partially) levels are denoted with solid lines. The unoccupied levels are denoted with dashed lines.

On top of the figure, four snapshots of the evolving cluster shapes are displayed. The solid vertical arrows mark the corresponding fragment separations. Observe that the doorway molecular configurations correspond to the second snapshot from the left. Notice the change in energy scale for the middle and bottom panels, as one passes from (o,s) to (s,s) and (p,s) final configurations.

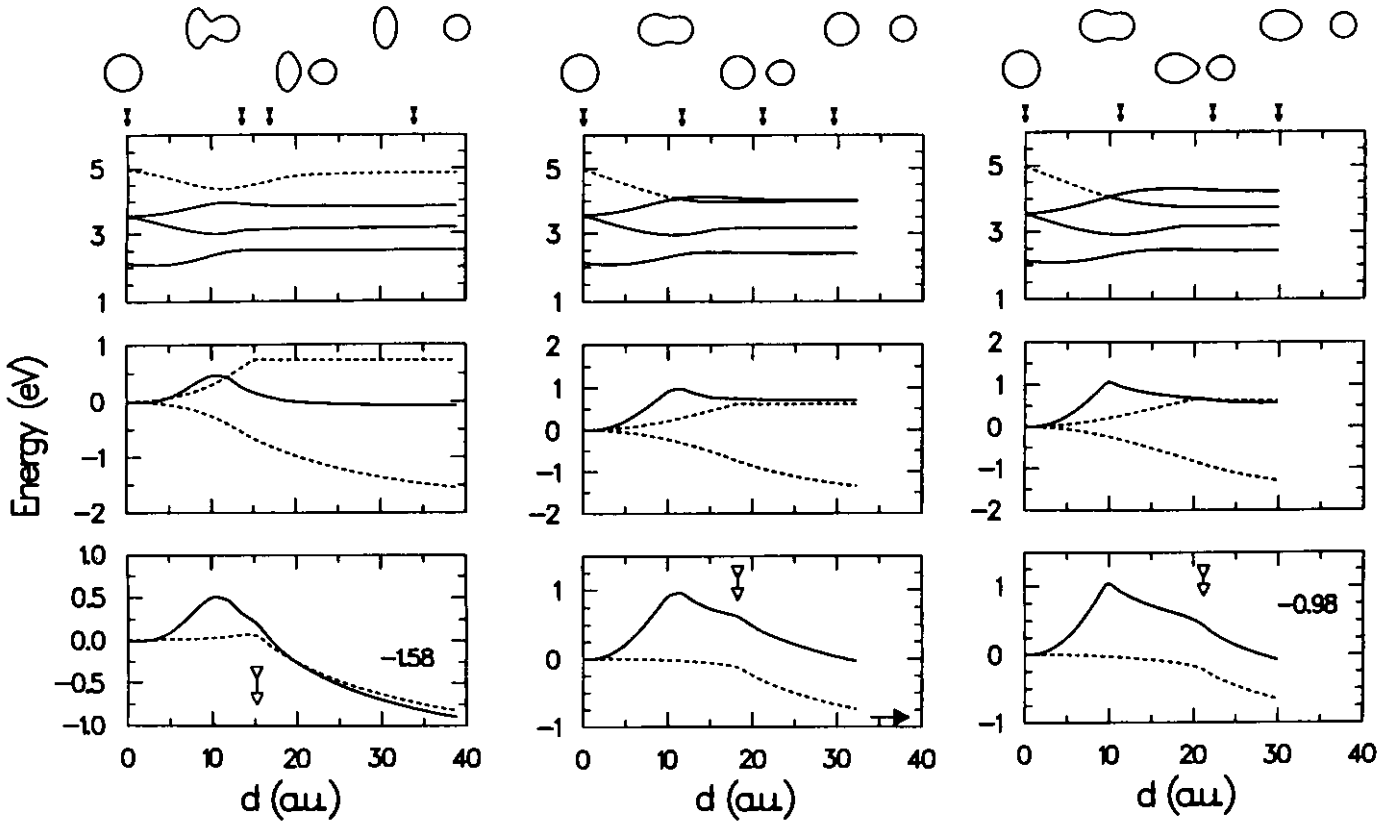
Energy (eV)
d (au)
d (au)
d (au)
-1.58
-0.98

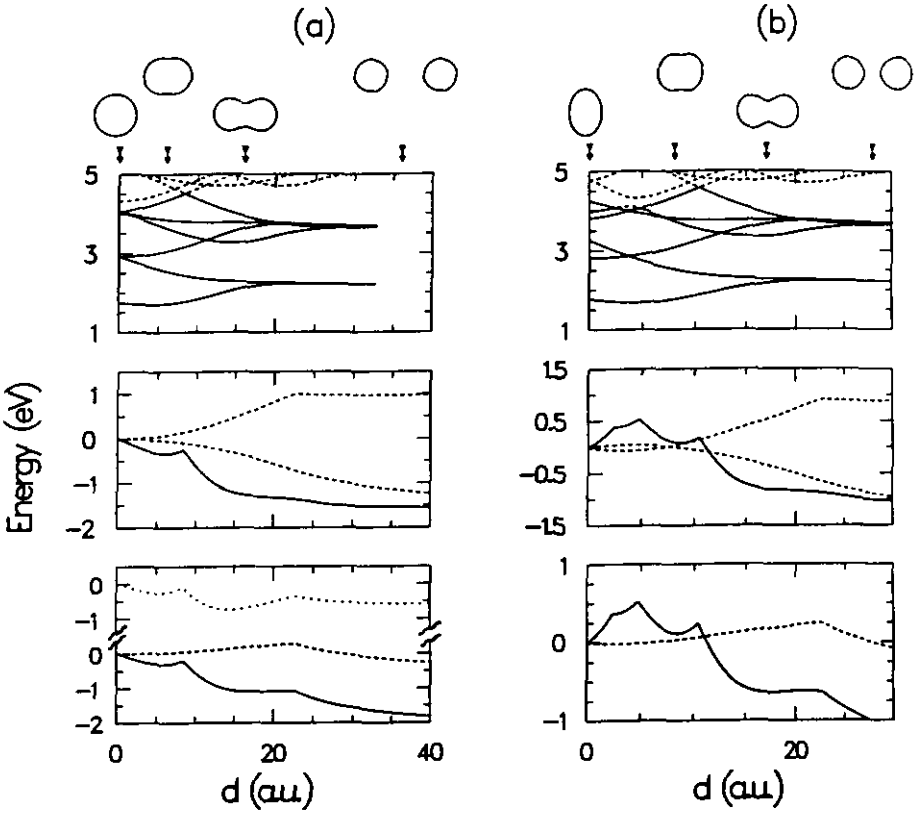

Fig. 22. ATCOSM results for the symmetric channel $Na_{18}^{2+} \rightarrow 2Na_9^+$, when the initial parent shape is assumed (a) spherical, and (b) oblate (with a shorter over longer axis ratio equal to 0.699). Panel distribution and other notations and conventions are the same as in Fig. 21. The top dotted line in the bottom panel of (a) represents the total energy without the Coulomb contribution. Observe that the doorway molecular configurations correspond to the third snapshot from the left. Notice that the zero of all energies is taken at $d = 0$.

tion into two Na_9^+ fragments. This gain is larger than the increase in energy (i.e., positive energy change) due to the surface term, which saturates at a value of about 1 eV after the scission point at $d \approx 23$ a.u. The total energy is displayed in the bottom panel of Fig. 22(a) (solid line) along with the LDM barrier (dashed line). Even though distorted (when compared to the cases of Fig. 21), the total barrier still exhibits a two-peak structure, the inner peak arising from the hump in the shell correction, and the outer peak arising from the point of saturation of the surface term (this last point coincides again with the scission point, as well as with the saddle of the LDM barrier). An inner local minimum is located at $d \approx 8$ a.u., and corresponds to a compact prolate shape of the parent [see second drawing from the left at the top of Fig. 22(a)], while a second deeper minimum appears at $d \approx 18$ a.u., corresponding to a superdeformed shape of a molecular configuration of two Na_9^+ clusters tied up together [preformation of fragments, see third drawing from the left at the top of Fig. 22(a)]. The inner barrier separating the compact prolate configuration from the superdeformed molecular configuration arises from the rearrangement of the single-particle levels during the transition from the initially assumed spherical Na_{18}^{2+} configuration to that of the supermolecule $Na_9^+ + Na_9^+$. We note that the barrier separating the molecular configuration from complete fission is very weak being less than 0.1 eV.

The top dotted line at the bottom panel displays the total energy in the case when the Coulomb contribution is neglected. This curve mimics the total energy for the fusion of two neutral Na_8 clusters, namely the total energy for the reaction $2Na_8 \rightarrow Na_{16}$. Overall, we find good agreement with a KS-LDA calculation for this fusion process (see Fig. 1 of Ref. [140]). We further note that the superdeformed minimum for the neutral Na_{16} cluster is deeper than that in the case of the doubly charged Na_{18}^{2+} cluster. Naturally, this is due to the absence of the Coulomb term.

The natural way for producing experimentally the metastable Na_{18}^{2+} cluster is by ionization of the stable singly charged Na_{18}^+ cluster. Since this latter cluster contains seventeen electrons and has a deformed oblate ground state [7], it is not likely that the initial configuration of Na_{18}^{2+} will be spherical or prolate as was assumed for illustration purposes in Fig. 22(a). Most likely, the initial configuration for Na_{18}^{2+} will be that of the oblate Na_{18}^+. To study the effect that such an oblate initial configuration has on the fission barrier, we display in Fig. 22(b) ATCOSM results for the pathway for the symmetric fission channel, starting from an oblate shape of Na_{18}^{2+}, proceeding to a compact prolate shape, and then to full separation between the fragments via a superdeformed molecular configuration. We

observe that additional potential humps (in the range 2 a.u. $\leq d \leq$ 6 a.u.), associated with the shape transition from the oblate to the compact prolate shape, develop for both channels. Concerning the total energies, the additional innermost humps result in the emergence of a significant fission barrier of about 0.52 eV for the favored symmetric channel [see $d \approx 5$ a.u. in Fig. 22(b)].

From the above analysis, we conclude that considerations of the energy pathways leading from the parent to preformation configurations (i.e., the inner-barrier hump, or humps) together with the subsequent separation processes are most important for proper elucidation of the mechanisms of metal-cluster fission processes. This corroborates earlier results obtained via *ab initio* molecular-dynamics simulations [43, 111, 8] pertaining to the energetics and dynamical evolution of fission processes, and emphasizes that focusing exclusively [132, 134] on the separation process between the preformed state and the ultimate fission products provides a rather incomplete description of fission phenomena in metal clusters. It is anticipated that, with the use of emerging fast spectroscopies, experimental probing of the detailed dynamics of such fission processes could be achieved.

This research was supported by a grant from the U.S. Department of Energy (Grant No. FG05-86ER45234). Calculations were performed on CRAY computers at the Supercomputer Center at Livermore, California, and the Georgia Institute of Technology Center for Computational Materials Science.

References

[1] Landman, U., Barnett, R.N., Cleveland, C.L., and Rajagopal, G. (1992) in *Physics and Chemistry of Finite Systems: From Clusters to Crystals*, eds. Jena, P., Khanna, S.N., and Rao, B.K., Kluwer Academic Publishers, Dordrecht, Vol. I, p. 165; Jortner, J. (1992) *Z. Phys. D* **24**, 247.

[2] Strutinsky, V.M. (1967) *Nucl. Phys. A* **95**, 420; (1968) **122**, 1.

[3] Preston, M.A. and Bhaduri, R.K. (1975) *Structure of the Nucleus*, Addison-Wesley, London.

[4] Yannouleas, C. and Landman, U. (1993) *Phys. Rev. B* **48**, 8376.

[5] Yannouleas, C. and Landman, U. (1993) *Chem. Phys. Lett.* **210**, 437.

[6] Barnett, R.N., Yannouleas, C., and Landman, U. (1993) *Z. Phys. D* **26**, 119.

[7] Yannouleas, C. and Landman, U. (1995) *Phys. Rev. B* **51**, 1902.

[8] Yannouleas, C., Barnett, R.N., and Landman, U. (1995) *Comments At. Mol. Phys.* **31**, 445.

[9] Yannouleas, C. and Landman, U. (1995) *J. Phys. Chem.*, in press.

[10] Koizumi, H., Sugano, S., and Ishii, Y. (1993) *Z. Phys. D* **28**, 223; Nakamura, M., Ishii, Y., Tamura, A., and Sugano, S. (1990) *Phys. Rev. A* **42**, 2267.

[11] Bulgac, A. and Lewenkopf, C. (1993) *Phys. Rev. Lett.* **71**, 4130.

[12] Frauendorf, S. and Pashkevich, V.V. (1993) *Z. Phys. D* **26**, S 98.

[13] Reimann, S.M., Brack, M., and Hansen, K. (1993) *Z. Phys. D* **28**, 235.

[14] Yannouleas, C. and Landman, U. (1994) *Chem. Phys. Lett.* **217**, 175.

[15] Bohr, Å. and Mottelson, B.R. (1975) *Nuclear Structure*, Benjamin, Reading, Massachusetts, Vol. II.

[16] Von Weizsäcker, C.F. (1935) *Z. Phys.* **96**, 431.

[17] Bethe, H.A. and Bacher, R.F. (1936) *Rev. Mod. Phys.* **8**, 82.

[18] Myers, W.D. and Swiatecki, W.J. (1966) *Nucl. Phys.* **81**, 1.

[19] Snider, D.R. and Sorbello, R.S. (1983) *Solid State Commun.* **47**, 845.

[20] Brack, M. (1989) *Phys. Rev. B* **39**, 3533.

[21] Serra, Ll., Garcías, F., Barranco, M., Navarro, J., Balbás, L.C., and Mañanes, A. (1989) *Phys. Rev. B* **39**, 8247.

[22] Membrado, M., Pacheco, A.F., and Sanūdo, J. (1990) *Phys. Rev. B* **41**, 5643.

[23] Engel, E. and Perdew, J.P. (1991) *Phys. Rev. B* **43**, 1331.

[24] Seidl, M., Meiwes-Broer, K.-H., and Brack, M. (1991) *J. Chem. Phys.* **95**, 1295.

[25] Yannouleas, C., Broglia, R.A., Brack, M., and Bortignon, P.F. (1989) *Phys. Rev. Lett.* **63**, 255.

[26] Yannouleas, C. and Broglia, R.A. (1991) *Phys. Rev. A* **44**, 5793; (1991) *Europhys. Lett.* **15**, 843; Yannouleas, C., Jena, P., and Khanna, S.N. (1992) *Phys. Rev. B* **46**, 9751.

[27] Yannouleas, C. (1992) *Chem. Phys. Lett.* **193**, 587.

[28] Yannouleas, C. and Broglia, R.A. (1992) *Ann. Phys.* (N.Y.) **217**, 105; Yannouleas, C., Vigezzi, E., and Broglia, R.A. (1993) *Phys. Rev. B* **47**, 9849; Yannouleas, C., Catara F., and Van Giai, N. (1995) *Phys. Rev. B* **51**, 4569.

[29] Kohn, W. and Sham, L.J. (1965) *Phys. Rev.* **140**, A1133.

[30] De Heer, W.A. (1993) *Rev. Mod. Phys.* **65**, 611.

[31] Kresin, V.V. (1992) *Phys. Rep.* **220**, 1.

[32] Ekardt, W. (1985) *Phys. Rev. B* **31**, 6360.

[33] Beck, D.E. (1991) *Phys. Rev. B* **43**, 7301.

[34] Harris, J. (1985) *Phys. Rev. B* **31**, 1770.

[35] Finnis, M.W. (1990) *J. Phys.: Condens. Matter* **2**, 331.
[36] Polatoglou, H.M. and Methfessel, M. (1988) *Phys. Rev. B* **37**, 10 403.
[37] Foulkes, W.M.C. and Haydock, R. (1989) *Phys. Rev. B* **39**, 12 520.
[38] Zaremba, E. (1990) *J. Phys.: Condens. Matter* **2**, 2479.
[39] Thomas, L.H. (1926) *Proc. Cambridge Philos. Soc.* **23**, 542; Fermi, E. (1928) *Z. Phys.* **48**, 73.
[40] Hodges, C.H. (1973) *Can. J. Phys.* **51**, 1428.
[41] Ekardt, W. (1984) *Phys. Rev. B* **29**, 1558.
[42] De Heer, W.A., Knight, W.D., Chou, M.Y., and Cohen, M.L. (1987) *Solid State Phys.* **40**, 93.
[43] Barnett, R.N., Landman, U., and Rajagopal, G. (1991) *Phys. Rev. Lett.* **67**, 3058; see also Barnett, R.N. and Landman, U. (1992) *ibid.* **69**, 1472; Barnett, R.N., Landman, U., Nitzan, A., and Rajagopal, G. (1991) *J. Chem. Phys.* **94**, 608; Cheng, H.-P., Barnett, R.N., and Landman, U. (1993) *Phys. Rev. B* **48**, 1820.
[44] Röthlisberger, U. and Andreoni, W. (1991) *J. Chem. Phys.* **94**, 8129.
[45] Perdew, J.P. and Zunger, A. (1981) *Phys. Rev. B* **23**, 5048.
[46] Balbás, L.C., Rubio, A., and Alonso, J.A. (1988) *Chemical Phys.* **120**, 239.
[47] Penzar, Z. and Ekardt, W. (1990) *Z. Phys. D* **17**, 69.
[48] Wood, D.M. (1981) *Phys. Rev. Lett.* **46**, 749.
[49] Van Staveren, M.P.J., Brom, H.B., de Jongh, L.J., and Ishii, Y. (1987) *Phys. Rev. B* **35**, 7749.
[50] Perdew, J.P. and Wang, Y. (1988) *Phys. Rev. B* **38**, 12 228.
[51] Siemens, Ph.J. and Jensen, A.S. (1987) *Elements of nuclei*, Addison-Wesley, New York.
[52] We emphasize that while the effective potentials are significantly different when SIC is used, other quantities, such as the total energy, IPs, and EAs are only slightly altered by SIC as shown in Ref. [45], and by our own calculations.
[53] Hofmann, S. 1989) *Proton radioactivity* in *Particle Emission from Nuclei*, eds. Poenaru, D.N. and Ivascu, M.S., CRC Press, Boca Raton, Florida, Vol. II, p. 25.
[54] Bréchignac, C., Cahuzac, Ph., Carlier, F., and Leygnier, J. (1989) *Phys. Rev. Lett.* **63**, 1368.
[55] Troullier, N. and Martins, J.L. (1992) *Phys. Rev. B* **46**, 1754; Martins, J.L., Troullier, N., and Weaver, J.H. (1991) *Chem. Phys. Lett.* **180**, 457.
[56] Kohanoff, J., Andreoni, W., and Parrinello, M. (1992) *Chem. Phys. Lett.* **198**, 472.
[57] Yabana, K. and Bertsch, G.F. (1993) *Physica Scripta* **48**, 633.
[58] Van Giai, N. and Lipparini, E. (1993) *Z. Phys. D* **27**, 193.
[59] Puska, M.J. and Nieminen, R.M. (1993) *Phys. Rev. A* **47**, 1181.
[60] Grammaticos, B. (1982) *Z. Phys. A* **305**, 257.
[61] Gallup, G.A. (1991) *Chem. Phys. Lett.* **187**, 187.
[62] Haddon, R.C., Brus, L.E., and Raghavachari, K. (1986) *Chem. Phys. Lett.* **125**, 459.
[63] Gerloch, M. and Slade, R.C. (1973) *Ligand field parameters*, Cambridge Univ. Press, London.
[64] Rosén, A. and Wästberg, B. (1989) *J. Chem. Phys.* **90**, 2525; Wästberg, B. and Rosén, A. (1991) *Physica Scripta* **44**, 276.
[65] Ye, L. and Freeman, A.J. (1992) *Chem. Phys.* **160**, 415.
[66] Due to the changing spill-out with excess charge z, the capacitance should be

written as $C + \delta(z)$. For our purposes here the small correction $\delta(z)$ can be neglected.

[67] Pederson, M.R. and Quong, A.A. (1992) *Phys. Rev. B* **46**, 13 584.

[68] Wang, Y., Tománek, D., Bertsch, G.F., and Ruoff, R.S. (1993) *Phys. Rev. B* **47**, 6711.

[69] Sai Baba, M., Lakshmi Narasimhan, T.S., Balasubramanian, R., and Mathews, C.K. (1993) *Int. J. Mass Spectrom. Ion Processes* **125**, R1.

[70] Hettich, R.L., Compton, R.N., and Ritchie, R.H. (1991) *Phys. Rev. Lett.* **67**, 1242.

[71] Limbach, P.A., Schweikhard, L., Cowen, K.A., McDermott, M.T., Marshall, A.G., and Coe, J.V. (1991) *J. Am. Chem. Soc.* **113**, 6795.

[72] For certain systems, such as for example sodium clusters, an orbitally-averaged-like SIC treatment yielded highest-occupied-molecular-orbital (HOMO) energies for anions in adequate agreement with the calculated electron affinities (see section 2.2.1 and Refs. [4, 5]).

[73] Cioslowski, J. and Raghavachari, K. (1993) *J. Chem. Phys.* **98**, 8734.

[74] Baz', A.I., Zel'dovich, Y.B., and Perelomov, A.M. (1969) *Scattering, reactions, and decay in nonrelativistic quantum mechanics*, Israel Program for Scientific Translations Ltd., Jerusalem.

[75] De Coulon, V., Martins, J.L., and Reuse, F. (1992), *Phys. Rev. B* **45**, 13 671.

[76] Knight, W.D., Clemenger, K., de Heer, W.A., Saunders, W.A., Chou, M.Y., and Cohen, M.L. (1984) *Phys. Rev. Lett.* **52**, 2141; (1984) **53**, 510(E).

[77] Ekardt, W. (1984) *Phys. Rev. B* **29**, 1558.

[78] Chou, M.Y., Cleland, A., and Cohen, M. L., (1984) *Solid State Commun.* **52**, 645.

[79] Beck, D.E. (1984) *Solid State Commun.* **49**, 381.

[80] Hund, F. (1927) *Linienspektren und Periodisches System der Elemente*, Springer, Berlin, p. 124 .

[81] Jahn, H.A. and Teller, E. (1937) *Proc. Roy. Soc.* (London), Ser. A, **161**, 220.

[82] Bohr, Å. and Mottelson, B.R. (1953) *K. Danske Vidensk. Selsk. Mat.-Fys. Medd.* **27**, no. 16.

[83] Nilsson, S.G. (1955) *K. Danske Vidensk. Selsk. Mat.-Fys. Medd.* **29**, no. 16.

[84] Clemenger, K.L. (1985) *Phys. Rev. B* **32**, 1359.

[85] Clemenger, K.L. (1985) *Ph.D. dissertation*, University of California, Berkeley.

[86] Saunders, W.A. (1986) *Ph.D. dissertation*, University of California, Berkeley.

[87] Eaton, J.G., Kidder, L.H., Sarkas, H.W., McHugh, K.M., and Bowen, K.H. (1992), in *Nuclear Physics Concepts in the Study of Atomic Cluster Physics*, R. Schmidt *et al* Eds., Springer, Berlin, *Lecture Notes in Physics* Vol. **404**, p. 291.

[88] Ekardt, W. and Penzar, Z. (1988) *Phys. Rev. B* **38**, 4273.

[89] We note, however, that triaxiality was incorporated in a KS-LDA calculation which was restricted to determination of the optimum shapes of the following four neutral sodium clusters, Na_{10}, Na_{12}, Na_{14}, and Na_{18} [see, Lauritsch, G., Reinhard, P.-G., Meyer, J., and Brack, M. (1991) *Phys. Lett. A* **160**, 179 and Brack, M. (1993) *Rev. Mod. Phys.* **65**, 677].

[90] Snider, D.R. and Sorbello, R.S. (1984) *Surf. Sci.* **143**, 204.

[91] Iachello, F., Lipparini, E., and Ventura, A. (1992), in *Nuclear Physics Concepts in the Study of Atomic Cluster Physics*, R. Schmidt *et al* Eds., Springer, Berlin, *Lecture Notes in Physics* Vol. **404**, p. 318;
Iachello, F. (1994) *Nucl. Phys. A* **570**, 145c.

[92] Barranco, M., Hernández, E.S., Lombard, R.J., and Serra, Ll. (1992) *Z. Phys. D*

22, 659.

[93] Bonačić-Koutecký, V., Fantucci, P., and Koutecký, J. (1991) *Chem. Rev.* **91**, 1035.

[94] Bréchignac, C., Cahuzac, Ph., Carlier, F., de Frutos, M., and Leygnier, J. (1992) *Chem. Phys. Lett.* **190**, 42.

[95] Borggreen, J., Chowdhury, P., Kebaili, N., Lundsberg-Nielsen, L., Lutzenkirchen, K., Nielsen, M.B., Pedersen, J., and Rasmussen, H.D. (1993) *Phys. Rev. B* **48**, 17 507.

[96] Bernath, M., Yannouleas, C., and Broglia, R.A., (1991)*Phys. Lett. A* **156**, 307

[97] Ekardt, W. and Penzar, Z. (1991) *Phys. Rev. B* **43**, 1322.

[98] Saunders, W.A. (1992) *Phys. Rev. A* **46**, 7028.

[99] Here, we consider clusters of monovalent elements (Na, K, and Cu). For polyvalent elements, N in Eq. (49) must be replaced by Nv, where v is the valency.

[100] For materials with high electronic densities, it is known that the usual LDA fails to provide correct values for the surface tension. Therefore, following Ref. [14], in the case of Cu clusters, we have carried an ETF calculation using the *stabilized-jellium*-LDA (SJ-LDA) functional.

[101] Gradshteyn, I.S. and Ryzhik, I.M. (1980) *Table of integrals, series, and products*, Academic, New York, ch. 8.11.

[102] Hasse, R.W. and Myers, W.D. (1988) *Geometrical relationships of macroscopic nuclear physics*, Springer-Verlag, Berlin, ch. 6.5.

[103] Nix, J.R. (1972) *Annu. Rev. Nucl. Part. Sci.* **22**, 65.

[104] Bhaduri, R.K. and Ross, C.K. (1971) *Phys. Rev. Lett.* **27**, 606.

[105] The perturbation $l^2 - < l^2 >_n$ in the hamiltonian (58) influences the shell correction ΔE_{sh}^{Str}, but not the average, $\widetilde{E}_{sp}$, of the single-particle spectrum, since $U_0 = 0$ for all shells with principal quantum number n higher than the minimum number required for accomodating N_e electrons (see, Ref. [15], p. 598 ff.).

[106] Homer, M.L., Honea, E.C., Persson, J.L., and Whetten, R.L. (unpublished).

[107] Pettiette, C.L., Yang, S.H., Craycraft, M.J., Conceicao, J., Laaksonen, R.T., Cheshnovsky, O., and Smalley, R.E. (1988) *J. Chem. Phys.* **88**, 5377.

[108] Bréchignac, C., Cahuzac, Ph., Leygnier, J., and Weiner, J. (1989) *J. Chem. Phys.* **90**, 1492.

[109] Iñiguez, M.P., Alonso, J.A., Aller, M.A., and Balbás, L.C. (1986) *Phys. Rev. B* **34**, 2152.

[110] López, J.M., Alonso, J.A., Garcias, F., and Barranco, M. (1992) *Ann. Physik* (Leipzig) **1**, 270.

[111] Bréchignac, C., Cahuzac, Ph., Carlier, F., de Frutos, M., Barnett, R.N., and Landman, U. (1994) *Phys. Rev. Lett.* **72**, 1636.

[112] Bréchignac, C., Cahuzac, Ph., Carlier, F., Leygnier, J., and Sarfati, A. (1991) *Phys. Rev. B* **44**, 11 386.

[113] Hill, D.L. and Wheeler, J.A. (1953) *Phys. Rev.* **89**, 1102.

[114] Knickelbein, M.B. and Yang, S. (1990) *J. Chem. Phys.* **93**, 5760.

[115] Whetten, R.L. and Schriver, K.E. (1989), in *Gas Phase Inorganic Chemistry*, Edited by D. H. Russell, Plenum Press, New York, p. 193.

[116] Selby, K., Vollmer, M., Masui, J., Kresin, V.V, de Heer, W.A., and Knight, W.D. (1989) *Phys. Rev. B* **40**, 5417.

[117] This broadening is due to thermal shape fluctuations [see, Yannouleas, C., Pacheco, J.M., and Broglia, R.A. (1990) *Phys. Rev. B* **41**, 6088], as well as to a temperature-independent process (referred to as Landau damping) which results from collec-

tive strength fragmentation due to couplings to incoherent particle-hole transitions ([25]-[28]). Microscopic calculations for the description of the latter process have been carried out primarily for closed-shell spherical clusters, with the exception of the open-shell neutral sodium clusters Na_6, Na_{10}, and Na_{12} (see, Ref. [96]; for a calculation regarding Na_{10}, see also Ref.[97]).

[118] Frost, W. (1973) *Theory of unimolecular reactions*, Academic, New York; see also: Scharf, D., Landman, U., and Jortner, J., (1986) *Chem. Phys. Lett.* **126**, 495; Scharf, D., Jortner, J., aud Landman, U. (1988) *J. Chem. Phys.* **88**, 4273; Kaukoneu, H.-P., Cleveland, C.L., and Landman, U. (1991) *J. Chem. Phys.* **95**, 4997; Schmidt, R., Seifert, G., and Lutz, H.O. (1991) *Phys. Lett.* **A158**, 231.

[119] (a) Bréchignac, C., Cahuzac, Ph., Carlier, F., and de Frutos, M. (1990) *Phys. Rev. Lett.* **64**, 2893; (b) Bréchignac, C. *et al.*, (1994) *Phys. Rev. B* **49**, 2825.

[120] Saunders, W.A. (1990) *Phys. Rev. Lett.* **64**, 3046; (1991) **66**, 840.

[121] Martin, T.P., Näher, U., Göhlich, H., and Lange, T. (1992) *Chem. Phys. Lett.* **196**, 113; Näher, U., Göhlich, H., Lange, T., and Martin, T.P. (1992) *Phys. Rev. Lett.* **68**, 3416.

[122] Bohr, N. and Wheeler, J.A. (1939) *Phys. Rev.* **56**, 426.

[123] Nix, J.R. and Swiatecki, W.J. (1965) *Nucl. Phys.* **71**, 1.

[124] Gamow, G. (1928) *Z. Phys.* **51**, 204.

[125] Coudon, E.U. and Gurney, R.W. (1928) *Nature* **122**, 439.

[126] Sandulescu, A., Poenaru, D.N., and Greiner, W. (1980) *Sov. J. Part. Nucl.* **11**, 528.

[127] Price, P.B. (1989) *Ann. Rev. Nucl. Part. Sci.* **39**, 19.

[128] For a theoretical review, see (1989) Greiner, W., Ivascu, M., Poenaru, D.N.. and Sandulescu, A. *Cluster radioactivities*, in *Treatise on Heavy-Ion Science*, edited by D.A. Bromley Plenum, New York, Vol. 8, p. 641.

[129] Nilsson, S.G. *et al.*, Nucl. Phys. (1969) **A131**, 1.

[130] Myers, W.D. and Swiatecki, W.J. (1966) *Nucl. Phys.* **81**, 1.

[131] Maruhn J., Greiner, W. (1972) *Z. Phys.* **251**, 431.

[132] Garcías, F., Alonso, J.A., Barranco, M., López, J.M., Mañanes, A., Németh, J. (1994) *Z. Phys. D* **31**, 275.

[133] Koizumi, H. and Sugano, S. (1995) *Phys. Rev. A* **51**, R886.

[134] Rigo, A., Garcías, F., Alonso, J.A., López, J.M., Barranco, M., Mañanes, A., Németh, J., in *Proceedings of ISSPIC7* (September 12-16, 1994, Kobe, Japan), to appear in Surface Letters and Reviews.

[135] The two-intersected-spheres jellium has also been used for describing the fusion of two neutral magic clusters (see Ref. [140]).

[136] In this three-variables parametrization, the B parameter controls the necking-in, the C parameter controls the distance, and the α parameter controls the asymmetry, leaving no freedom for the shapes of the parent or the emerging fragments to be varied. In particular, both parents remain simultaneously either prolatelike or oblatelike, while final spherical shapes are excluded altogether. The weaknesses of the "funny hills" parametrization with respect to metal-cluster fission have been discussed in Näher, U., Frank, S., Malinowski, N., Zimmermann, U., Martin, T.P. (1994) *Z. Phys. D* **31**, 191.

[137] Mustafa, M.G., Mosel, U., Schmitt, H.W. (1973) *Phys. Rev. C* **7**, 1519.

[138] (1965) *Handbook of mathematical functions*, edited by Abramowitz, M. and Segun, I.A., Dover, New York.

[139] Jennings, B.K. (1973) *Nucl. Phys. A* **207**, 538; Jennings, B.K., Bhadhuri, R.K.,

Brack, M. (1975) *Phys. Rev. Lett.* **34**, 228.

[140] Knospe, O., Schmidt, R., Engel, E., Schmitt, U.R., Dreizler, R.M., Lutz, H.O. (1993) *Phys. Lett. A* **183**, 332.